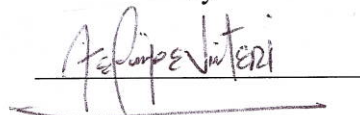


Diagnostics for a Supersonic Wind Tunnel

A Major Qualifying Project Report
Submitted to the Faculty of the
WORCESTER POLYTECHNIC INSTITUTE
in Partial Fulfillment of the Requirements for the
Degree of Bachelor of Science
in Aerospace Engineering

by



David Viteri



Lydia Johnston



Shea Bernardo

March 25, 2015

Approved by:



Professor John J. Blandino, Advisor
Aerospace Engineering Program
Mechanical Engineering Department, WPI

Abstract

The goal of this project was to design and improve existing diagnostics for the indraft supersonic wind tunnel (SWT) at Worcester Polytechnic Institute. Diagnostics include a pitot system to measure static and stagnation pressures which can then be used to calculate Mach number, and a schlieren system for visualizing wave structures in the flow. Pitot system design and electronics used for the data acquisition system were evaluated. LabVIEW code for obtaining a Mach number using pressure measurements was written and validated through benchtop, testing. The schlieren optical system was also modified to improve image brightness, contrast, and resolution as well as to facilitate positioning of optical components. Schlieren system images were compared with pressure gradient results produced by a previous design group using computational fluid dynamics software and showed qualitative agreement.

“Certain materials are included under the fair use exemption of the U.S. Copyright Law and have been prepared according to the fair use guidelines and are restricted from further use.”

Acknowledgements

The group would like to thank the following individuals for their assistance on this project:

Professor Blandino – for his guidance throughout the course of the project.

Mik Tan and the Washburn Machine Shop – for his assistance in machining all of the parts needed for the project.

Professor Im – for his guidance in designing and assessing the schlieren system.

Zach Taillefer – for his assistance in using equipment for assessing and fixing electronics.

Table of Authorship

| Section | Author |
|--------------------------------------------|--------|
| Abstract | All |
| Introduction | LJ |
| Background Information | |
| 2.1 Wind Tunnel | SB |
| 2.2 Schlieren System | DV |
| 2.3 Pitot System | LJ |
| Methodology | |
| 3.1 Schlieren System | LJ |
| 3.2 Pitot System | SB |
| 3.3 Qualification Test Plan | DV |
| 3.4 Manufacturing | DV |
| Results | |
| 4.1 Schlieren System | LJ, DV |
| 4.2 Pitot System | LJ, SB |
| 4.4 Future Work | LJ, SB |
| Appendices | |
| 6.1 Test Calculations of Mach Number Error | SB |
| 6.2 Single Mirror Off-Axis Design | LJ |
| 6.3 LabVIEW VI Instructions | LJ |

| | |
|-------------------------------------------|----|
| 6.4 Voltage Transfer Function Python Code | LJ |
| 6.5 Newton Raphson MATLAB Code | LJ |
| 6.6 Fsolve MATLAB Code | LJ |

Table of Contents

| | |
|-----------------------------------------------------------|----|
| Abstract..... | 1 |
| Acknowledgements..... | 2 |
| Table of Authorship | 3 |
| Table of Contents..... | 5 |
| List of Figures | 7 |
| List of Tables | 9 |
| 1. Introduction..... | 10 |
| 1.1. Project Description..... | 10 |
| 1.2. Project Goals | 10 |
| 2. Background Information..... | 12 |
| 2.1. Wind Tunnel Design | 12 |
| 2.1.1. Intermittent Indraft Wind Tunnel..... | 12 |
| 2.1.2. Previous Work..... | 12 |
| 2.2. Schlieren System | 17 |
| 2.2.1. History..... | 17 |
| 2.2.2. Scientific Principles | 17 |
| 2.2.3. Z-type Configuration | 19 |
| 2.2.4. Previous Work: 2013 MQP..... | 22 |
| 2.2.5. Previous Work: 2014 MQP..... | 29 |
| 2.3. Pitot System | 32 |
| 2.3.1. Subsonic Pitot Systems | 32 |
| 2.3.2. Supersonic Rayleigh Pitot Formula | 33 |
| 2.3.3. Critical Pressure Ratio..... | 35 |
| 2.3.4. Shock Standoff Distance | 36 |
| 2.3.5. Previous Work: 2013 MQP..... | 39 |
| 3. Methodology | 42 |
| 3.1. Schlieren System | 42 |
| 3.1.1. Schlieren Configurations..... | 42 |
| 3.1.2. First Stage..... | 46 |
| 3.1.3. Image Capture..... | 52 |
| 3.1.4. System Mounting..... | 55 |
| 3.1.5. Single Mirror Off-Axis, Configuration 2015.2 | 59 |
| 3.2. Pitot System | 61 |
| 3.2.1. Pressure Probe Installation..... | 61 |
| 3.2.2. Pressure Transducers..... | 63 |
| 3.2.3. Data Acquisition System (DAQ) | 65 |
| 3.2.4. Test of DAQ System | 70 |
| 3.3. Manufacturing..... | 73 |
| 3.3.1. CAD Models..... | 73 |
| 3.3.2. CAM Models..... | 74 |
| 3.3.3. Machining | 76 |
| 3.4. Qualification Test Plan | 76 |

| | |
|-----------------------------------------------------------------------------------------------------|----|
| 4. Results..... | 79 |
| 4.1. Schlieren System | 79 |
| 4.2. Pitot System | 84 |
| 4.3. Recommendations for Future Work | 86 |
| 4.3.1. Schlieren System..... | 86 |
| 4.3.2. Pitot System | 87 |
| 5. References | 89 |
| 6. Appendices | 91 |
| 6.1. Test Calculations of Mach number Error for Honeywell #HSCDANN001BAAA3 Pressure Transducer..... | 91 |
| 6.2. Single Mirror Off-Axis Design | 93 |
| 6.3. LabVIEW VI Instructions | 95 |
| 6.4. Voltage Transfer Function Python Code | 96 |
| 6.5. Newton Raphson MATLAB Code | 97 |
| 6.6. Fsolve MATLAB Code..... | 98 |
| 6.6.1. Main Function | 98 |
| 6.6.2. Fsolve Function | 98 |

List of Figures

| | |
|------------------------------------------------------------------------------------------------------------|----|
| Figure 1. 2010 SWT Design [2] Copyright 2010 Kelly Butler, et al..... | 14 |
| Figure 2. Wind Tunnel Set-up [1]. Copyright 2014 by Katlin Davis et al..... | 16 |
| Figure 3. Wind Tunnel Test Section [1]. Copyright 2014 by Katlin Davis et al..... | 16 |
| Figure 4. Z-type Schlieren Configuration [6] Copyright 2003 by Vanessa Krake et al. (UMN Physics) | 20 |
| Figure 5. Light collimation between concave mirrors | 21 |
| Figure 6. X-Channel Mounting Adapter [4] Copyright 2013 by William Bugden et al..... | 22 |
| Figure 7. StockerYale Imagelite Mite Model 20 [4] Copyright 2013 by William Bugden et al. | 23 |
| Figure 8. 2013 Condenser Lens Assembly [4] Copyright 2013 by William Bugden et al. | 24 |
| Figure 9. 2013 SWT Slit Assembly [4] Copyright 2013 by William Bugden et al. | 25 |
| Figure 10. 2013 Concave Mirror Assembly [4] Copyright 2013 by William Bugden et al. | 26 |
| Figure 11. 2013 Knife Edge and Vernier Assembly [4] Copyright 2013 by William Bugden et al. | 27 |
| Figure 12. 2013 Focusing Lens Assembly [4] Copyright 2013 by William Bugden et al. | 27 |
| Figure 13. 2013 Image Projection Screen [4] Copyright 2013 by William Bugden et al..... | 28 |
| Figure 14. 2013 Camera and Lens [4] Copyright 2013 by William Bugden et al. | 28 |
| Figure 15. 2013 z-type Schlieren System [4] Copyright 2013 by William Bugden et al..... | 29 |
| Figure 16. 2014 Light Source Assembly | 29 |
| Figure 17. 2014 Slit and Screen Design..... | 30 |
| Figure 18. 2014 Optical Plate CAD Model [1] Copyright 2014 by Katlin Davis et al. | 31 |
| Figure 19. Subsonic Pitot System [8] Copyright 2008 by MIT..... | 32 |
| Figure 20. Pressure Measurements in a Supersonic Flow [8] Copyright 2008 by MIT..... | 34 |
| Figure 21. Rayleigh Pitot Formula Relation | 35 |
| Figure 22. Shock Standoff Distance vs. Mach Number for 1/16 in OD Tubing..... | 38 |
| Figure 23. 2013 Pressure Port Configuration [4] Copyright 2013 by William Bugden et al. | 39 |
| Figure 24. Front Panel of the 2013 LabVIEW VI [4] Copyright 2013 by William Bugden et al. | 41 |
| Figure 25. Schlieren Configuration 2014.1 | 43 |
| Figure 26. Schlieren Configuration 2015.1 | 44 |
| Figure 27. Schlieren Configuration 2015.2 | 45 |
| Figure 28. Schlieren Configuration 2015.3 | 46 |
| Figure 29. Old Condenser Lens Angle Comparison..... | 47 |
| Figure 30. Old System Light Collimation | 47 |
| Figure 31. DCX Lens Focal Length Comparison..... | 49 |
| Figure 32. Flat Mirror and Mount | 50 |
| Figure 33. Updated Slit Design..... | 51 |
| Figure 34. Final slit design..... | 52 |
| Figure 35. Single mirror low shutter speed | 54 |
| Figure 36. Single mirror high shutter speed (1/4000 s)..... | 54 |
| Figure 37. Single mirror direct capture, 1/60s shutter speed | 54 |
| Figure 38. Screen capture test, off-axis single mirror, 1/60s shutter speed | 55 |
| Figure 39. X-Channel Mounting System..... | 56 |
| Figure 40. Magnet Mirror Mount Cutaway CAD, 1-1/4in Diameter, 1-1/2in Height | 57 |
| Figure 41. Mirror mount with magnet..... | 58 |

| | |
|--------------------------------------------------------------------------------------------------------------------------------------------|----|
| Figure 42. DCX Lens with new mirror mount..... | 58 |
| Figure 43. Flexible, galvanized steel sheets | 59 |
| Figure 44. Harvard Natural Sciences Demonstrations single mirror setup [15] Copyright 2013 by Harvard Natural Sciences Demonstrations..... | 60 |
| Figure 45. Off-axis single mirror with existing optics | 60 |
| Figure 46. Probe Alignment Fixture Model, 5/8 x 1 x 2-1/4 inches | 62 |
| Figure 47. Pressure Transducer Circuit Box | 64 |
| Figure 48. DAQ Assistant and Time calculation | 66 |
| Figure 49. LabVIEW Voltage Transfer Function | 68 |
| Figure 50. Final LabVIEW Front Panel | 69 |
| Figure 51. Newton Raphson Solver in LabVIEW | 70 |
| Figure 52. Test Setup Reference Diagram [4] Copyright 2013 by William Bugden et al. | 71 |
| Figure 53. Initial Test Setup | 71 |
| Figure 54. DAQ Card Channel Inputs | 72 |
| Figure 55. Tools utilized in ESPRIT | 75 |
| Figure 56. Configuration 2015.2 with candle, minor reflective issues | 79 |
| Figure 57. Light focused on slit, 2x back focal length | 80 |
| Figure 58. Light at 2x BFL with slit..... | 80 |
| Figure 59. Light at 2x BFL without slit | 80 |
| Figure 60. Light focused on slit, 4x back focal length | 81 |
| Figure 61. Schlieren Configuration 2015.3 Setup | 81 |
| Figure 62. Image with flat mirror with +40% contrast..... | 82 |
| Figure 63. Fluent Schlieren Image at a pressure ratio of 10 [1] Copyright 2014 by Katlin Davis et al..... | 82 |
| Figure 64. DBN Schlieren Test, Lower Contrast | 83 |
| Figure 65. DBN Schlieren Test, Higher Contrast | 84 |
| Figure 66. Expected pressure-voltage relation | 85 |
| Figure 67. Single Mirror Design..... | 93 |
| Figure 68. Sample LabVIEW output in Excel | 95 |

List of Tables

| | |
|-------------------------------------------------------------------------------|----|
| Table 1. 2013 List of Optical Components | 23 |
| Table 2. Finalized First Stage Distances | 49 |
| Table 3. Initial camera capture testing results, off-axis single mirror | 54 |
| Table 4. Initial DAQ Test Results | 72 |

1. Introduction

1.1. Project Description

The main objective of this project was to implement and test two diagnostic tools for the existing, indraft style, supersonic wind tunnel that interfaces with the T2 vacuum chamber at Worcester Polytechnic Institute (WPI). An additional task was to commission the wind tunnel and the diagnostics for use in testing and research. The first diagnostic tool is a pitot system used to measure static and stagnation pressures in the tunnel to allow calculation of Mach number in the test section. The second diagnostic tool is a schlieren system, which uses the differential refraction of light due to density gradients to image flow structures in high speed gas flows. Additional deliverables include usage and maintenance documentation for the wind tunnel and diagnostic tools.

1.2. Project Goals

The main objectives of this project were divided into three elements, namely the wind tunnel, the pitot system, and the schlieren system. Supporting objectives for each category are defined below.

Wind Tunnel Goals

The wind tunnel in its present form is the culmination of refinement over the course of five years of work by undergraduate students at WPI. The ultimate goal of the project is to provide a reliable facility to run tests of nozzle contours or small scale models in supersonic flows with a duration on the order of tens of seconds. Leaks have been an issue in the past, so another goal is to anticipate where future leaks may occur and implement countermeasures. It is possible

that future users may encounter leaks, therefore providing troubleshooting documentation in this area is necessary.

Pitot System Goals

The goal for the pitot system is construct, install, and test a pitot sensor and transducer, as well as to provide a reliable method for post-processing static and stagnation pressure data to track the Mach number in the test section over time. Both the pitot system and schlieren system should run in parallel, meaning that the two systems must not interfere with each other. Ideally, the probe's configurations should require only minimal disassembly of the tunnel to install. Finally, a method for reliably bending the stagnation probe and accurately aligning it parallel to the direction of flow must be designed and implemented.

Schlieren System Goals

The goal for the schlieren system is to refine the existing one such that it can produce images that allow qualitative boundary layer characterization and possibly quantitative measurements of shock and expansion wave angles. A Computational Fluid Dynamics (CFD) model, developed by a previous group, provides an estimate of the expected flow field which can then be compared to the schlieren images to evaluate the sensitivity of the system and help interpret the results. Ideally, the schlieren system images should require minimal post-processing to enhance contrast and brightness. Finally, the schlieren system should require minimal adjustment of optical components between tests.

2. Background Information

2.1. Wind Tunnel Design

The diagnostic tools in this project are designed to interface with an existing supersonic wind tunnel designed and built by previous Major Qualifying Project (MQP) groups [1] [2] [3] [4]. This wind tunnel is an intermittent indraft type tunnel attached to the T2 vacuum chamber in WPI's Vacuum Testing Facility (VTF) as seen in Figure 2.

2.1.1. Intermittent Indraft Wind Tunnel

Air flow in this type of wind tunnel is generated as a result of the pressure difference between ambient air (at the tunnel inlet) and lower pressure air inside the vacuum chamber (at the outlet). In order to generate this pressure difference, the vacuum chamber is sealed by a valve, and then pumped down until the pressure is in the range of tens of millitorr. The valve is then opened, allowing the air to flow in (i.e. "indraft") through the wind tunnel test section and into the vacuum chamber. However, the flow will cease once the pressure in the vacuum chamber equals the ambient pressure. In addition, the flow in the test section will not remain supersonic for its entire duration. This leaves a finite window of test time, during which useful data can be collected.

2.1.2. Previous Work

The following sections summarize the contributions of each of the previous projects towards the design and construction of this supersonic wind tunnel. Each section title corresponds to the time frame in which each project was carried out.

Summer 2009

During the summer of 2009, WPI student Peter Moore was tasked with the design and fabrication of a small-scale supersonic wind tunnel suitable for teaching and research purposes at WPI [3]. After extensive research and analysis of the different types of supersonic wind tunnels and consideration of time and budget constraints, an indraft tunnel design was chosen primarily due to the availability of the VTF vacuum chamber on-site. The final design consisted of a mounting flange to attach the wind tunnel to a port on the vacuum chamber, two identical contoured plates which would serve as the top and bottom of the tunnel sandwiched between two transparent acrylic sheets, and a lever-operated ball valve at the inlet. The contours were designed to simulate the two dimensional shape of a converging-diverging nozzle. The ideal contour profile was calculated using an algorithm based on the method of characteristics. Moore had begun fabricating the components, but was unable to finish assembly and testing of the wind tunnel before graduation.

Academic Year 2009-2010

The 2010 MQP group was tasked with completing the supersonic wind tunnel started by Moore. Moore's design featured only one tunnel configuration, which for a properly functioning wind tunnel would produce a flow with a single, nominal, "design" Mach number in the test section. In order to experiment with flows of different Mach numbers, this group was tasked with designing a wind tunnel with a variable contour system [2]. This rather complex design is shown in Figure 1. The assembly of Moore's wind tunnel was completed and tested, exposing the flaws. The group's own design was refined to address those flaws. The original tunnel suffered from leaks which rendered it inoperable as a test facility. Since the ball valve is located at the

inlet of the tunnel, any leaks in the test section prevented the vacuum chamber from generating the necessary pressure difference while being pumped down.

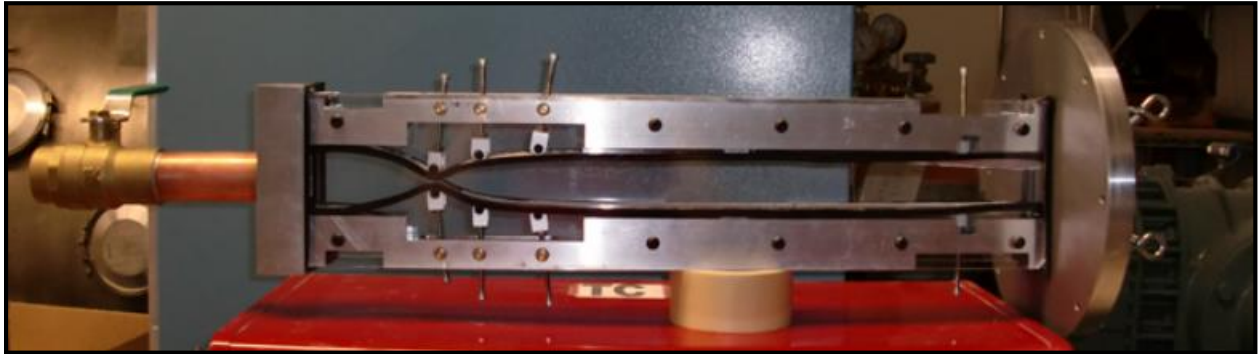


Figure 1. 2010 SWT Design [2] Copyright 2010 Kelly Butler, et al.

The ball valve assembly, the side window design, and the cross-sectional area dimensions of Moore's tunnel were reused in the group's final design. Rubber o-rings were inserted between the ends of the test section, and the valve and flange assemblies. A rubber sealing strip was also installed between the flexible contour plates and the acrylic plates as a measure against potential leaks observed in the original tunnel. Unfortunately, the new wind tunnel configuration also suffered leaking and the mounting flange was found to be poorly manufactured. Due to the extensive and time-consuming nature of the manufacturing and assembly process, there was no time remaining to further test the new tunnel.

Academic Year 2012-2013

The 2013 group was tasked with continuing work on the wind tunnel based on the previous groups' efforts with the exception of the complex, adjustable test section. The mounting flange was refurbished; the ball valve assembly was reused; and the test section was redesigned with similar cross-sectional area and some added length. The new test section consisted of an upper and lower contoured piece held together by two endplates and tightly

sandwiched between two acrylic sheets [4]. This design bears more similarities to Moore's tunnel than the 2010 one. However, the new design included rubber o-rings between the contours and the windows, as well as o-rings at the endplates. The o-rings were fitted into grooves to prevent them from sliding out of place. In addition, the endplates were sealed to the contour pieces with a silicon adhesive.

Following final testing, one last-minute modification was made to be implemented by future groups. The upper and lower contour pieces of the test section were replaced with upper and lower brackets with separate contour plates fastened to each [4]. This allowed the contours to be interchangeable, requiring barely any disassembly to replace the contours without interfering with any seals. Therefore, new contours could be fabricated and easily interchanged, as needed.

Academic Year 2013-2014

Unlike the previous groups, the 2014 group was not tasked with designing and constructing a supersonic wind tunnel. Rather, the group's objective required the use of the previously designed tunnel to test flow through a specific nozzle profile: the dual-bell nozzle [1]. Along the way, several improvements to the wind tunnel were made. The assembly of the new modular test section, designed last-minute in the previous project, was completed. The new design allowed the old contours to be swapped out with new ones fabricated to simulate the profile of a dual-bell nozzle. Damage to the acrylic sheets was observed where the sheets were screwed to the brackets; therefore, the group replaced the acrylic with polycarbonate, which has a greater compression strength. To prevent leaks, vacuum grease was applied to the o-rings, and the brackets and endplates were sealed together with silicone caulk [1].

Figure 2 and Figure 3 show the supersonic wind tunnel from the 2014 project which was the starting point for this project.

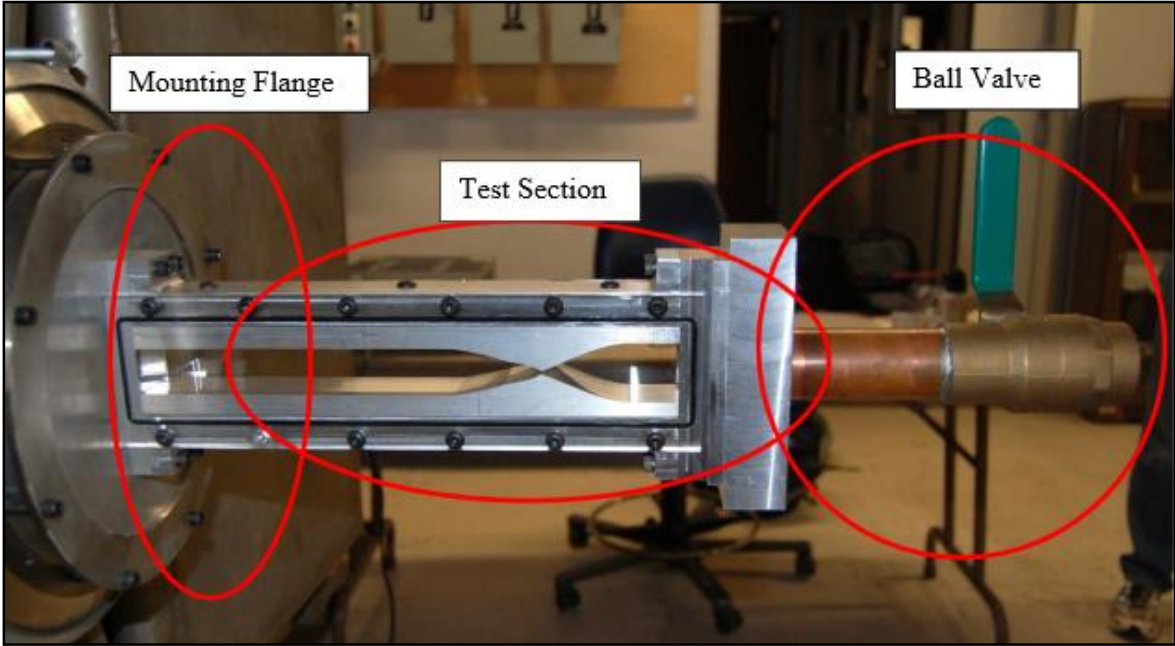


Figure 2. Wind Tunnel Set-up [1]. Copyright 2014 by Katlin Davis et al.

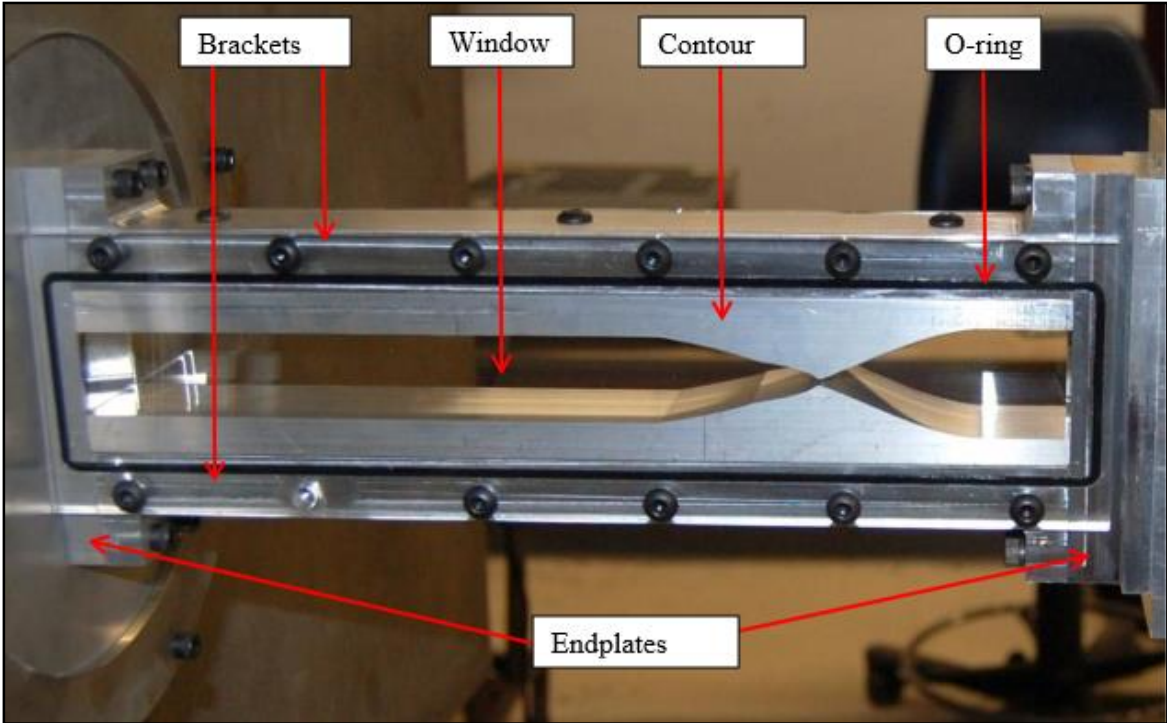


Figure 3. Wind Tunnel Test Section [1]. Copyright 2014 by Katlin Davis et al.

2.2. Schlieren System

2.2.1. History

Robert Hooke's experiment with a candle and a lens in the 17th century proved optical systems to be useful diagnostic tools for the investigation of gaseous flows [5]. This technique, later named schlieren photography, utilizes density gradients in order to investigate phenomena that occur in inhomogeneous media. Hooke's original setup was very simple yet innovative for his time; he used one candle as the light source, a lens to focus the image, and his eye to capture it. This configuration changed and improved throughout the years thanks to great minds like Foucault, Toepler and Mach, who added mirrors, a knife edge and the idea of visualizing supersonic flows respectively [5].

Further significant improvements and new applications appeared in the 20th century with Prandtl and Meyer. The applications of schlieren photography now extended to recording oblique shocks in a supersonic flow, ballistic and rocket analysis, and study of wing sections undergoing transonic and supersonic speeds. With WWII the utilization of schlieren techniques to determine airflows around rockets and missiles was fundamental, in this period the refinement of this technique reached its peak. The most recent application of schlieren photography was developed by Weinstein in 1993 and consisted of utilizing a telescope and recording flights of supersonic aircraft as far as 10km away [5].

2.2.2. Scientific Principles

The general principle behind schlieren photography is a simple phenomenon: the refraction of light rays. The refractive index varies through inhomogeneous media, which means

light does not propagate uniformly. Such changes in the refractive index can be expressed with the following equation [5]:

$$n = \frac{c_o}{c} \quad (2.2.1)$$

Where c_o is the universal speed of light in vacuum and c is the speed of light in the medium [5]. Similarly for gases, there is a very simple expression relating the refractive index with the gas' density, ρ . The equation is the following [5]:

$$n - 1 = k\rho \quad (2.2.2)$$

In this expression, k is the Gladstone-Dale coefficient and is typically $0.23 \text{ cm}^3/\text{g}$ for air at standard conditions. The value $(n - 1)$ is known as refractivity, which is a measure of how much a material will bend the light propagating through it. For air, this value is 0.000292 [5]. Refractivity is more pronounced for liquids and solids than gases. Additionally, refractivity depends significantly on the properties of the gas, such as: density, temperature and pressure, as well as the wavelength of the light.

Is important to create a mathematical model for the schlieren system that will help better understand the principle behind it. Some relationships that represent the changes in the refractive index are needed in order to create this model. The mathematical relationships are referenced to a Cartesian coordinate system with the z-axis in the direction of the propagation of light rays before they enter inhomogeneous media.

According to Settles' book [5], which is one of the most complete references available on the topic of schlieren imaging, "it can be demonstrated that optical inhomogeneities refract or bend light rays in proportion to their gradients of refractive index in an x-y plane". The following differential equations represent the ray curvature in both the x and y directions [5]:

$$\frac{\partial^2 x}{\partial z^2} = \frac{1}{n} \frac{\partial n}{\partial x} \quad , \quad \frac{\partial^2 y}{\partial z^2} = \frac{1}{n} \frac{\partial n}{\partial y} \quad (2.2.3)$$

After integration, the angular ray deflection ¹in the x and y directions (ε_x and ε_y , respectively) become [5]:

$$\varepsilon_x = \frac{1}{n} \int \frac{\partial n}{\partial x} \partial z \quad , \quad \varepsilon_y = \frac{1}{n} \int \frac{\partial n}{\partial y} \partial z \quad (2.2.4)$$

In a 2D case of length L along the z-axis this equation becomes [5]:

$$\varepsilon_x = \frac{L}{n_o} \frac{\partial n}{\partial x} \quad , \quad \varepsilon_y = \frac{L}{n_o} \frac{\partial n}{\partial y} \quad (2.2.5)$$

In this instance, n_o is the refractive index of the surrounding medium. The refraction of light is mainly caused by the refractive index gradients in both the x and y directions characteristic of an inhomogeneous region.

2.2.3. Z-type Configuration

There are several ways to configure a schlieren system, depending on the space constraints and the desired image quality. The most common type of configuration is the “z-type” which is what the 2013 MQP decided to start with [4]. The set-up is based on William Herschel’s idea of tilting his telescope’s parabolic mirror off its axis in order to obtain a better image. The figure below shows the elements and specific set-up of the components in the z-type configuration.

¹ The effect of light when its rays are bent in a certain angle due to a change in the refractive index

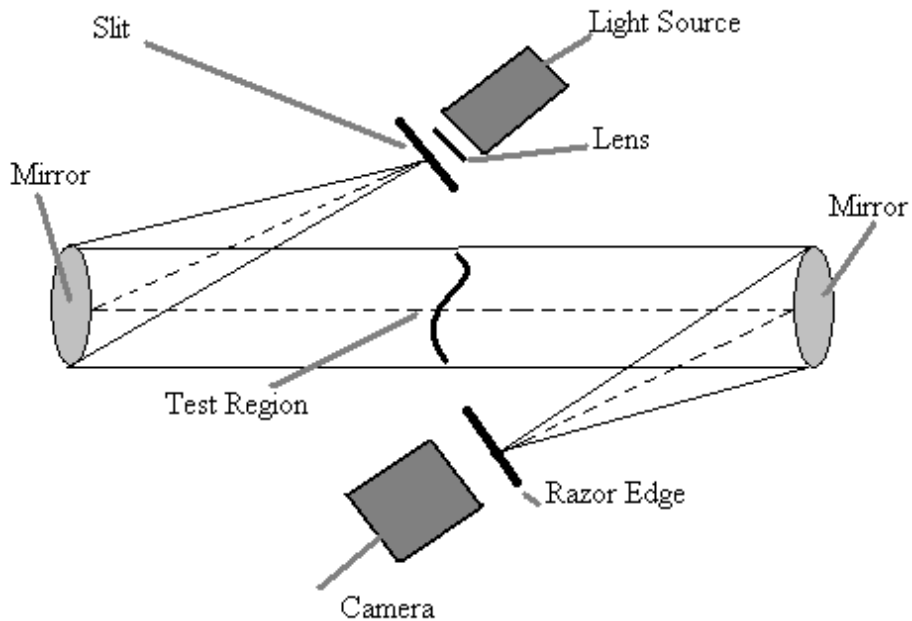


Figure 4. Z-type Schlieren Configuration [6] Copyright 2003 by Vanessa Krake et al. (UMN Physics)

Figure 4 shows the light path along the system forming a “Z,” hence the name of this schlieren configuration. The z-type system can be split into three stages. In the first stage, the light path begins at the source, then passes through a condenser lens which focuses the beam into a point. Then the light passes through a slit and diverges again into the first concave mirror. The slit is important to help with the contrast of the picture by making the light rays unidirectional. The concave mirror’s main function is to collimate the light rays in order to make them parallel through the test section, which is effectively the second stage of the z-type. The third stage is where the light is converged again by using a second concave mirror after the test region. Before the final image is obtained it is important that half of the light rays are blocked by the razor edge as shown in Figure 4. The razor edge is essential because it blocks a fraction of the

light rays in order to show the density gradient changes in the test section. It is also important to take into account that the minimum possible distance between the two mirrors is than twice their focal length, as shown in the figure below:

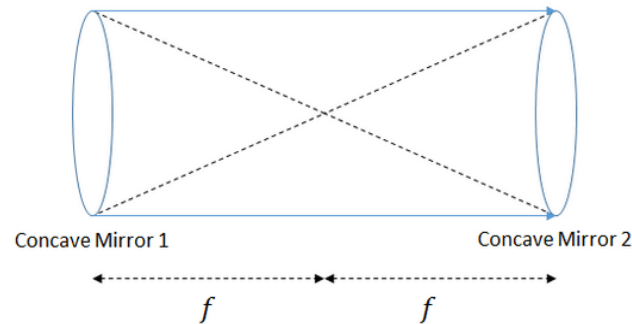


Figure 5. Light collimation between concave mirrors

Finally, off-axis optical systems may suffer from aberrations such as coma and astigmatism² that can affect the quality of the image. An aberration is where light rays fails to focus on a single point. One of the great advantages of the z-type configuration is that it doesn't suffer from coma since it's cancelled due to the utilization of two mirrors. Nonetheless, the z-type configuration will still experience some astigmatism effects, which can at least be reduced by aligning the optical components accurately. The current configuration for the schlieren system is the z-type. This configuration was implemented in past projects due to its popularity and the abundance of literature related to it [5], as well as the reduction of the coma aberration.

² Coma is a lens aberration that creates blurred edges of a projected object. Astigmatism is a lens aberration caused by having different lens curvatures on different planes creating a defect on the projected object.

2.2.4. Previous Work: 2013 MQP

The 2013 supersonic wind tunnel (SWT) project was the first one to implement the schlieren system as a diagnostic tool [4]. The z-type configuration described above was chosen and remains the configuration in use. In order to mount all of the optical components, X-Channel, and designed adapters were utilized that would fit the custom 8-32 threaded rods into the ¼-20 threaded posts for support. Figure 6 below shows an example of the adapter used to mount the aspheric condenser lens on the X-Channel.



Figure 6. X-Channel Mounting Adapter [4] Copyright 2013 by William Bugden et al.

Additionally an optical mounting table was designed and constructed in order to avoid any vibrations from the tunnel itself, and the X-Channel rods were placed on this table. The entire assembly is provided in Figure 15 on page 29.

The components used for the system are summarized in Table 1.

| | |
|------------------------|-------------------------------------|
| Light source | StockerYale Imagelite Mite Model 20 |
| Condenser Lens | Thorlabs - ACL 2018 |
| Slit | N/A |
| 2 Concave Mirrors | Thorlabs – CM508-200-F01 |
| Knife Edge and Vernier | N/A & Thorlabs – DH1 |
| Focusing Lens | Thorlabs - AC508-250-A |
| Screen | N/A |

Table 1. 2013 List of Optical Components

The light source chosen for the schlieren system was an Imagelite Mite Model 20 (StockerYale Inc., now ProPhotonix Ltd.). The light source control box has a knob to regulate the intensity of the light. This light source uses a fiber optic, adjustable gooseneck cable to channel the light from the control box to the desired location. Figure 7 shows the Imagelite Mite Model 20.



Figure 7. StockerYale Imagelite Mite Model 20 [4] Copyright 2013 by William Bugden et al.

The condenser lens chosen was an aspheric lens, model ACL 2018, from Thorlabs, Incorporated. The lens has a diameter of 20 mm and a relatively short focal length of 18mm. This proved to be an issue with the mirror and is discussed in Section 3.1.2. Figure 8 shows the assembly used by the 2013 team to support the condenser lens.



Figure 8. 2013 Condenser Lens Assembly [4] Copyright 2013 by William Bugden et al.

The next component is the slit. A section of eraser shield and taped construction paper on the edges was used in order to block any stray light that could interfere. Its dimensions are not stated in the paper, the only thing they mentioned was the orientation of the slit which is vertical. Figure 9 shows the slit machined by the 2013 group [4].



Figure 9. 2013 SWT Slit Assembly [4] Copyright 2013 by William Bugden et al.

The next two components are the concave mirrors. The first mirror collimates the divergent light from the slit. The collimated light from the first mirror is directed through the wind tunnel test section, where it is refracted due to density gradients in the air. The second mirror reflects and focuses this collimated light toward the knife edge, discussed later. The mirrors were purchased from Thorlabs. Both mirrors have a diameter of 2 in (50.8mm) and focal length of 200mm. As mentioned earlier in Section 2.2.3, the distance between the two concave mirrors must be no less than twice their focal length, so for these mirrors the length of the test section must be a minimum of 40cm. The mirrors are parabolic, UV enhanced, and have an aluminum coating. The decision to pick these mirrors was made based on the project's budget as well as the size of the wind tunnel. These mirrors were the best match for the project specifications given the available resources. Figure 10 shows the assembly that was used to support the concave mirrors.



Figure 10. 2013 Concave Mirror Assembly [4] Copyright 2013 by William Bugden et al.

The knife edge utilized in the 2013 schlieren system was an assembly consisting of a razor blade with a vernier adjustment to control the height, the vernier was purchased from Thorlabs and the model number is DH1. This assembly enabled easy control of the percentage of light cut off and the distance of the knife edge from the second mirror. Theoretically, 50% of the light rays should be cut off for an ideal case. Additionally, a focusing lens from Thorlabs, model No. AC508-250-A, was purchased in order to condense the light while maintaining image quality. The focusing lens has a diameter of 2 in (50.8mm) and a focal length of 250mm. Figure 11 and Figure 12 below show the setup for the knife edge vernier assembly as well as the focusing lens for the 2013 schlieren system.



Figure 11. 2013 Knife Edge and Vernier Assembly [4] Copyright 2013 by William Bugden et al.



Figure 12. 2013 Focusing Lens Assembly [4] Copyright 2013 by William Bugden et al.

Finally, the image was projected into a screen and recorded with a camera. The makeshift screen was a clipboard with a sheet of Dell Premium Photo Paper for the projection surface. This paper provides a smoother surface to reduce the scattering of light when it hits the paper, which results in a crisper image [4]. The camera utilized to take the pictures was a Lumix DMC-GF3 and the

lens was a Lumix G Vario 14-44mm. Pictures for both of these components are shown in Figure 13 and Figure 14 below.



Figure 13. 2013 Image Projection Screen [4] Copyright 2013 by William Bugden et al.



Figure 14. 2013 Camera and Lens [4] Copyright 2013 by William Bugden et al.

The final setup with all of the components assembled and aligned is shown in Figure 15 below.



Figure 15. 2013 z-type Schlieren System [4] Copyright 2013 by William Bugden et al.

2.2.5. Previous Work: 2014 MQP

There were several major improvements made to the schlieren system by the 2014 SWT team [1]. These improvements were designed to resolve problems involving stability of the components and misalignment of the focal points. Starting with the light source, a cylindrical bracket was machined to hold the light source fiber optic cable in a fixed, stable, position. Additionally the bracket was designed to be tightened into a threaded aluminum post. Figure 16 shows the results of the changes to the light source mounting system.



Figure 16. 2014 Light Source Assembly

The next two components improved were the slit and the projection screen. It was concluded that the 2013 slit and screen materials were not the best option in order to get a clear image. A CAD model and new pieces for the slit and the screen were generated. The new parts would have a matte finish in order to help diffuse any reflection of light. Figure 17 shows the slit and projection screen fabricated by the 2014 group.



Figure 17. 2014 Slit and Screen Design

The mirror assembly was modified as well. The intent was to improve the stability of the system, as the team experienced “wobbly” mirrors. It was decided to put the mirrors in ball and socket mounts. This altered the mirror heights, so new aluminum rod posts for the new mounts were designed and machined.

The largest improvement in 2014 was replacing the X-Channel configuration with a solid aluminum optical plate. The main reason for this change was the misalignment of the components. The required distances and angles for an optimal configuration were determined;

and with these numbers a CAD model, shown in Figure 18, was designed. For reference, the bottom of the plate measures 36 inches across.

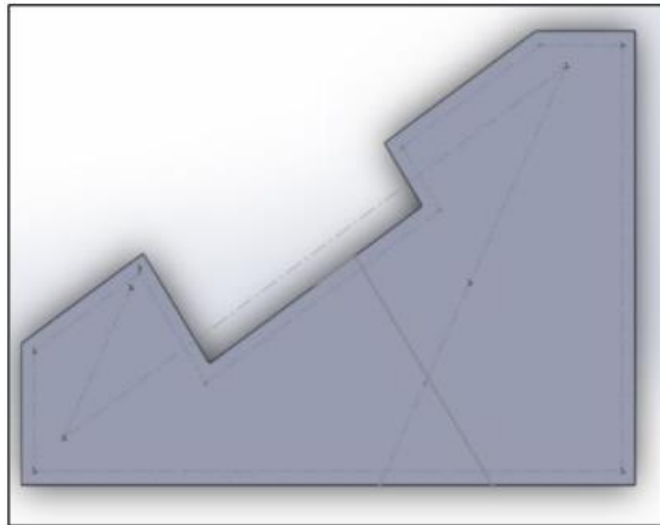


Figure 18. 2014 Optical Plate CAD Model [1] Copyright 2014 by Katlin Davis et al.

There are components that are meant to be free to move and others are firmly attached to the plate. The movable components are the slit, the knife edge assembly and the screen. All of the movable components structurally support themselves and do not need to be attached to the optical plate. The fixed components are: the light source, condenser lens, concave mirrors and focusing lens.

2.3. Pitot System

2.3.1. Subsonic Pitot Systems

Pitot-static systems are used to determine the velocity and Mach number of airflow [7]. They can be installed on an aircraft to measure airspeed, or a wind-tunnel to measure the free stream velocity and Mach number in the test section. The first part of a pitot-static system is the stagnation probe, oriented parallel to the direction of flow, which measures the total (or “stagnation”) pressure p_0 . The second part is the static probe, which is oriented perpendicular to the direction of the flow, either on the stagnation probe or on a side wall of the wind tunnel. The static probe measures the static pressure in the flow p . The pitot-static system configuration is shown in Figure 19.

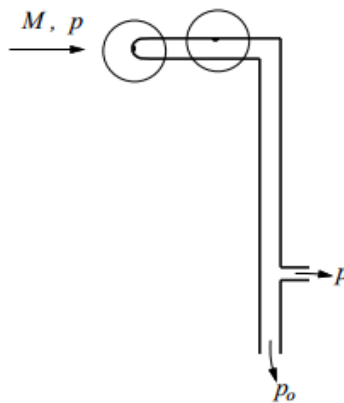


Figure 19. Subsonic Pitot System [8] Copyright 2008 by MIT

For subsonic conditions, the pitot-static system operates on Bernoulli’s principle, which states that the sum of the static pressure and dynamic pressure equals the total pressure [8]:

$$p + \frac{\rho V^2}{2} = p_0 \quad (2.3.1)$$

This expression can be solved for the velocity V in terms of the pressure difference measured by pressure transducers and air density ρ :

$$V = \sqrt{\frac{2(p_0 - p)}{\rho}} \quad (2.3.2)$$

However, Bernoulli's equation (Equation 2.3.2) is only valid for low, incompressible Mach numbers of 0.3 or lower. For higher subsonic Mach numbers, the stagnation and static pressure ratio can be found using discrete pressure measurements. Measuring the pressure ratio enables computation of the Mach number using the isentropic p_0/p relation [8]:

$$\frac{p_0}{p} = \left(1 - \frac{\gamma - 1}{2} M^2\right)^{\gamma/(\gamma - 1)} \quad (2.3.3)$$

In this case, M is the test section Mach number, and γ is the specific heat ratio, which for this project can be approximated as 1.4 since the gas is (diatomic) air.

2.3.2. Supersonic Rayleigh Pitot Formula

Implementing a pitot system in a supersonic test section introduces complexities to the subsonic problem. When the flow is supersonic, a detached bow shock develops in front of the pitot tube, as shown below.

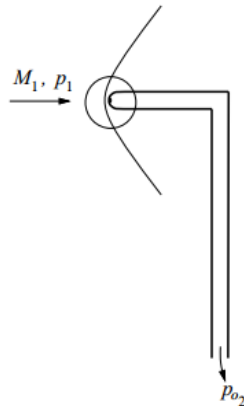


Figure 20. Pressure Measurements in a Supersonic Flow [8] Copyright 2008 by MIT

The flow streamlines across the normal portion of the shock are decelerated nonisentropically to a subsonic Mach number, and then isentropically decelerated to zero inside the stagnation probe, measured as P_{02} in Figure 20 [9]. Because the stagnation pressure measured is for the subsonic flow behind the normal shock, the isentropic relation (Equation 2.3.3) used in the subsonic case cannot be applied across the shock. Instead, Equation 2.3.3 behind the bow shock would look like:

$$\frac{p_{02}}{p_2} = \left(1 - \frac{\gamma - 1}{2} M_2^2\right)^{\gamma/(\gamma-1)} \quad (2.3.4)$$

Note that the above relation is function of M_2 , the Mach number downstream of the shock, while the desired Mach number is M_1 , located upstream of the shock. The portion of the shock immediately in front of the stagnation probe inlet may be approximated as a normal shock. This means that normal shock relations may be used to relate the ratio of static pressure upstream of the shock (p_1) and stagnation pressure downstream of the shock (p_{02}) to the desired Mach number M_1 . This relation is called the *Rayleigh Pitot Formula* [8]:

$$\frac{P_{02}}{P_1} = \left(\frac{\gamma + 1}{2} M_1^2\right)^{\frac{\gamma}{\gamma-1}} \left/\left(\frac{\gamma + 1}{1 - \gamma + 2\gamma M_1^2}\right)^{\frac{1}{\gamma-1}}\right. \quad (2.3.5)$$

The utility of this formula lies in the fact that discrete measurements of the stagnation pressure downstream of the shock and the static pressure upstream of the shock can be used to find the Mach number in the test section for Mach numbers above unity. This is a complex function to solve for the Mach number, but numerical solution methods in MATLAB enable computation of the Mach number for a given pressure ratio p_{02}/p_1 . Several MATLAB scripts were written using

both “fsolve” tools in MATLAB and Newton-Raphson methods discussed below to develop a tool for solving for the supersonic Mach number based on pressure measurements. The code for both methods may be found in Appendix 6.5 and 6.6. Figure 21 shows a plot of the “fsolve” function over a range of Mach numbers from 1.4-2.6. These calculations were made assuming γ is a constant equal to 1.4.

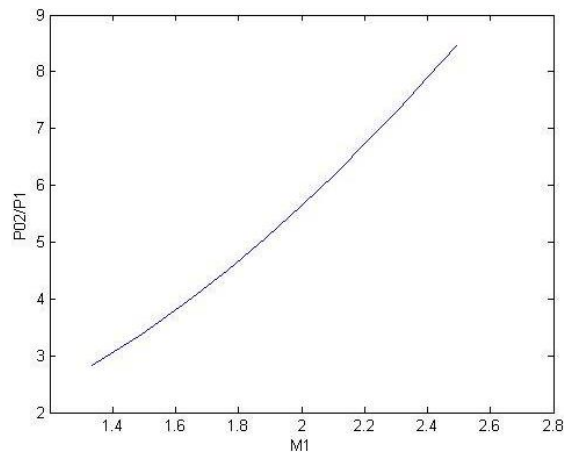


Figure 21. Rayleigh Pitot Formula Relation

Results from the fsolve method (Appendix 6.6) were compared with Newton-Raphson MATLAB solver written by the 2013 team (Appendix 6.5) [4]. Both methods result in the same correlation between pressure ratio and Mach number.

2.3.3. Critical Pressure Ratio

Another complex part of this problem is that supersonic wind tunnels are capable of both subsonic and supersonic Mach numbers, which means that in order to know which relation to use for the Mach number, the flow regime in the test section must be known. The critical pressure ratio for sonic conditions, where the Mach number is at unity, is described by the following Equation [9]:

$$\frac{p^*}{p_0} = \frac{2}{\gamma + 1} \frac{\gamma}{\gamma - 1} \quad (2.3.6)$$

For this project, taking γ as 1.4, the critical pressure ratio is ≈ 0.528 [9]. Therefore, if the ratio of the measured static to total pressure is lower than this critical pressure ratio, then the flow is supersonic and the Rayleigh Pitot Formula must be used in lieu of the isentropic relation to calculate the Mach number. The critical pressure ratio was confirmed using the Virginia Tech Compressible Aerodynamics Calculator [10]. Using the Normal Shock Relations calculator for a supersonic Mach number approaching unity, (e.g. $M = 1.0001$), $p_1/p_{02} \approx 0.52822$. The isentropic relations for the subsonic condition also approach this value. For a Mach number of 1, the Isentropic Flow Relations calculator returns a pressure ratio $p_1/p_{01} \approx 0.52828$. Note that for a pressure ratio of 0.528, both relations yield a similar Mach number of ≈ 1 , so either relation is reasonably valid around unity. This critical pressure ratio was later implemented in the LabVIEW script, described in Section 3.2.3.

2.3.4. Shock Standoff Distance

In the previous (2013) design, the static ports were located on the bottom contour of the wind tunnel (see Figure 23 on page 39) [4]. A similar configuration was chosen for this design, as discussed later in Section 3.2. These static ports experience boundary layer effects, which were neglected for this analysis. The location of the static port along the test section is critical, because it must be as close to where the bow shock develops as possible without being downstream of it. The distance between a blunt body and the detached bow shock is known as the shock

standoff distance. Empirical evidence shows that the standoff distance is approximately linearly related to the inverse density ratio across the shock, as shown below [11]:

$$\frac{\Delta}{R} \approx 1.1 \left(\frac{\rho_1}{\rho_2} \right) \quad (2.3.7)$$

In this expression, Δ represents the shock standoff distance, R is the radius of the blunt body, and ρ_1 and ρ_2 are the static densities upstream and downstream of the shock, respectively.

The static density ratio is related to the free stream Mach number as follows [11]:

$$\frac{\rho_1}{\rho_2} = \frac{(\gamma + 1)M_1^2}{(\gamma - 1)M_1^2 + 2} \quad (2.3.8)$$

Substituting Equation 2.3.8 into Equation 2.3.7 and solving for Δ , the shock standoff distance becomes:

$$\Delta = R \left(1 + 1.1 \frac{(\gamma - 1)M_1^2 + 2}{(\gamma + 1)M_1^2} \right) \quad (2.3.9)$$

The probe design, as will be described in Section 3.2, uses 1/16 in OD tubing. Using 1/32 in as R , a MATLAB plot was generated for the shock standoff distance as a function of Mach number:

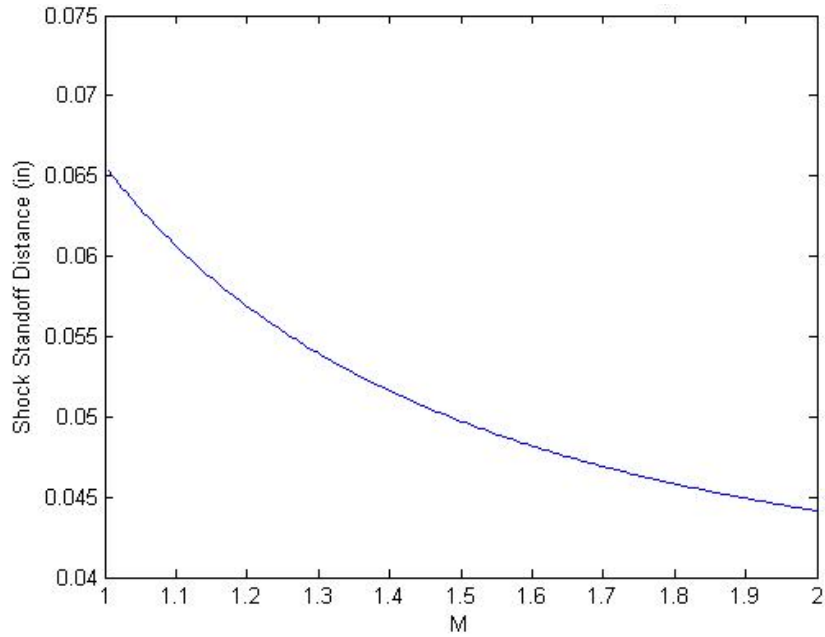


Figure 22. Shock Standoff Distance vs. Mach Number for 1/16 in OD Tubing

The shock standoff distance increases as the Mach number decreases, with a maximum distance of .065 inches when the Mach number is at unity. Note that according to Equation 2.3.9, at unity, the shock standoff distance is 2.1 times the radius of the object. However, it is expected that the shock standoff distance will not actually reach this limiting value as the Mach number approaches unity, which is not reflected by this relation [11]. While more accurate methods would be ideal, this relation provides an order of magnitude estimate of the shock standoff distance. A common practice for determining the actual shock standoff distance involves running tests with a schlieren system to empirically determine its location. These data may be supplemented by simulations using CFD tools.

2.3.5. Previous Work: 2013 MQP

A preliminary pitot system was designed for the supersonic wind tunnel as part of the 2013 project [4]. The design had the stagnation probe inserted into the test section through the acrylic side panel and held in place with epoxy. Four static ports were permanently drilled through the contour into the bottom of the test section. Each port had a Swagelok NPT to compression tube fitting, where a 1/16 in OD, 1/50 in ID steel tube was press fit into the NPT and adjusted to be flush with the aluminum contour inside the test section. This steel tube was attached to flexible tubing, which then connected to a pressure transducer.

There are several issues with the current pitot system components outlined in the 2013 MQP team's paper. First, the LabVIEW code that determined the flow regime in the wind tunnel (discussed in Section 3.2.3) doesn't work reliably. Another issue mentioned was that the rubber tubes connecting the pressure ports and transducers would pinch shut during chamber evacuation. Using a stiff material for the tubes could potentially solve this issue.



Figure 23. 2013 Pressure Port Configuration [4] Copyright 2013 by William Bugden et al.

The pressure transducer selected as part of the 2013 project for both static and stagnation pressure measurements was Honeywell's TruStability® #HSCDANN001BAAA3. This sensor provides a ±1% full scale error band, meaning measurements are within ±1% of the full range of measurement [12]. The pressure range of this sensor was 0-100kPa, which means each measurement is within 1kPa of the actual pressure. According to the analysis presented in the 2013 project, this uncertainty in the pressure measurement results in a ±0.1 uncertainty in the calculated Mach number [4]. This calculation was performed again with similar results as described in Section 3.2.2 using the methodology outlined in Appendix 6.1.

The relation used to calculate the pressure from voltage measured by the transducer is provided by the Honeywell Company [12]:

$$V_{output} = \frac{0.8V_s}{p_{max} - p_{min}} (p_a - p_{min}) + 0.1V_s \quad (2.3.10)$$

In this expression, V_s is the supplied voltage, V_{output} is the measured voltage, p_{max} is the maximum pressure (atmospheric pressure, 101kPa), and p_{min} is the minimum measurable pressure (0 kPa). Solving for the applied pressure, p_a , provides the following relation:

$$p_a = 1.25p_{max} \left(\frac{V_{output}}{V_s} \right) - 0.125p_{max} \quad (2.3.11)$$

This expression was implemented in LabVIEW in order to compute the pressures from the measured voltages. The pressure ratio was then computed using these discrete pressure measurements, and a Newton Raphson method was applied to the Rayleigh Pitot Formula to solve for the test section Mach number. The LabVIEW VI displayed the measured pressures and the computed Mach number:

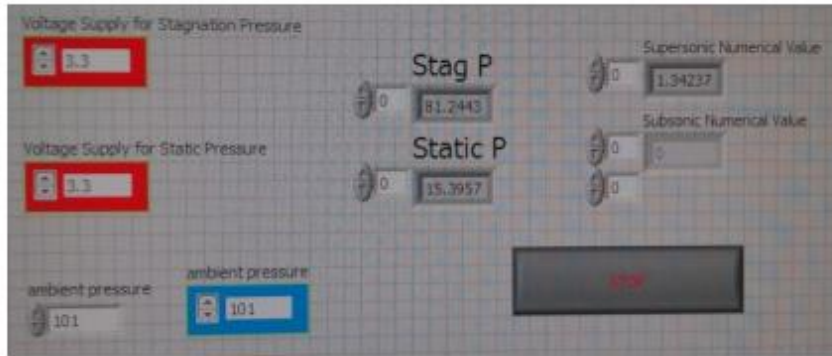


Figure 24. Front Panel of the 2013 LabVIEW VI [4] Copyright 2013 by William Budgen et al.

3. Methodology

3.1. Schlieren System

This section describes the process used to improve the quality of the schlieren system. Major areas for improvement included image brightness and contrast. Assessment of improvement in this area required qualitative comparison of results to both previous results and results predicted by computational fluid dynamics. The design of this system was driven by validation tests every time an optical component was changed or a new element was added. This led to several different configurations, described in Section 3.1.1 and used throughout this section explain testing. In general, calculations were made to find distances between optical components, but ultimately, using the schlieren system requires physical adjustments to achieve the desired results. This section details these preliminary tests, and the Results section describes the final testing and conclusions.

The z-type system can be broken up into three stages, which are described in the following three subsections. The first stage includes the light source, condenser lens, slit, and first mirror, and is discussed in Section 3.1.2. The second stage includes the collimated light between the two mirrors; this second stage also includes the test section where the wind tunnel resides. The third stage includes the second mirror, knife edge, and capturing plane, and is discussed in Section 3.1.3.

3.1.1. Schlieren Configurations

Configuration 2014.1

The following diagram shows the schlieren configuration for the 2014 project. It consists of two major stages and the test section in the middle. The first stage consists of the light source, condenser lens, slit and first concave mirror. The second stage consists of the second concave mirror, the razor edge, and the screen.

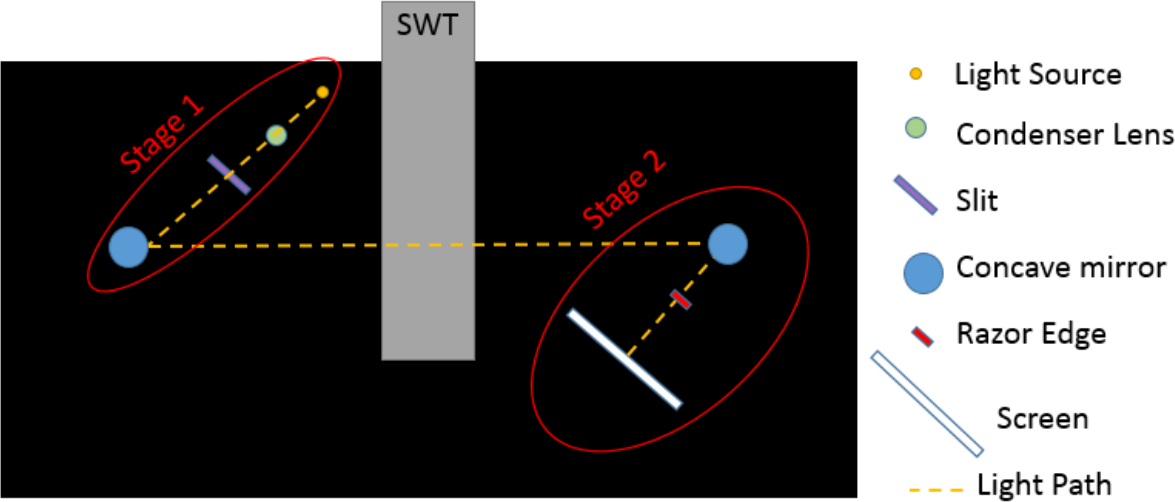


Figure 25. Schlieren Configuration 2014.1

Configuration 2015.1

The first attempt was to create a single mirror configuration shown in the figure below. The major reason to use this one was because the setup was easier and the results were better. The only problem with it were the off-axis aberrations.

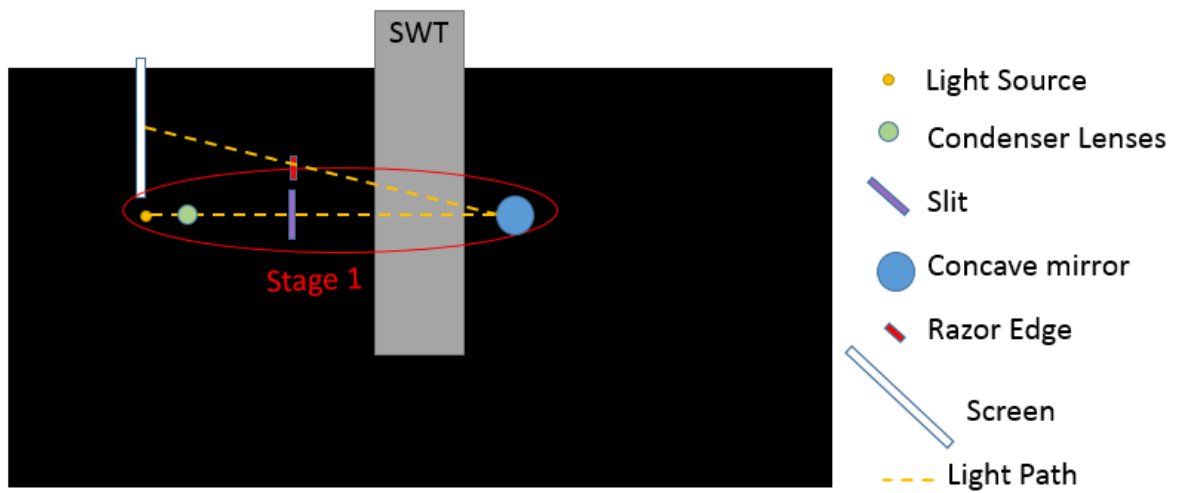


Figure 26. Schlieren Configuration 2015.1

Configuration 2015.2

The redesigned z-type system included a new condenser lens as well as new orientation of the components in order to fit them in the table. This new condenser lens will be further discussed in the following sections. This is what the second configuration looked like.

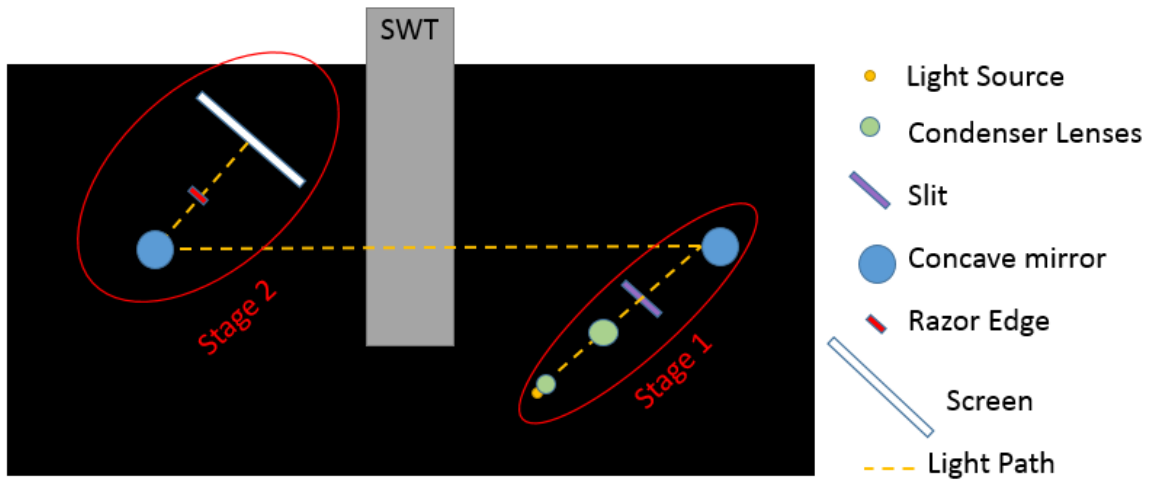


Figure 27. Schlieren Configuration 2015.2

Configuration 2015.3

The last configuration that was tested included a flat mirror in order to make a better use of the space in the optical table as well as to have less crowded test area. This flat mirror was introduced in the first stage and it helped break it in smaller segments. The configuration is shown in the figure below.

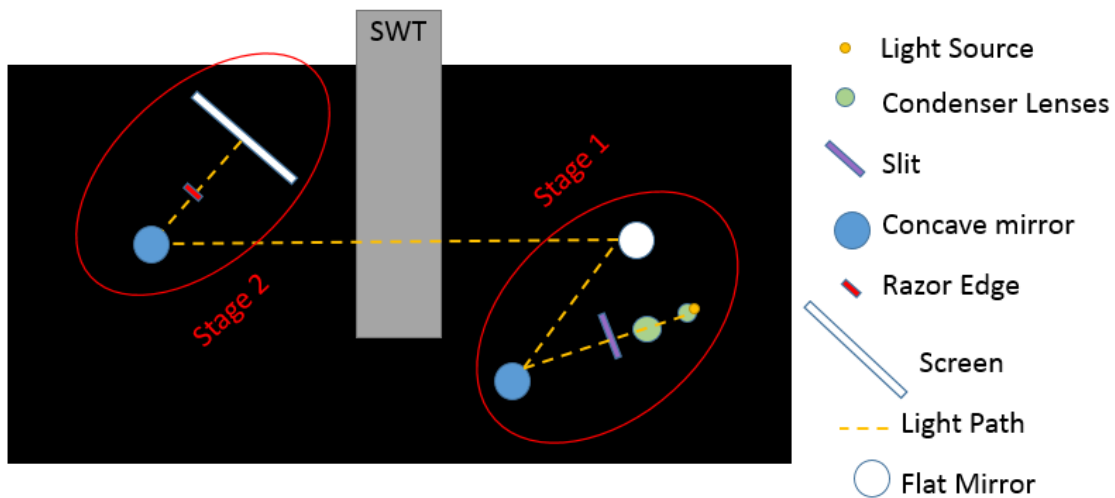


Figure 28. Schlieren Configuration 2015.3

3.1.2. First Stage

One of the main issues with the previous z-type system was the loss of large amounts of light in the first stage. This was because of the incompatibility of the condenser lens and collimating mirror. In order for the mirror to collimate the light correctly, the angle of the incoming rays needed to match the ratio between the published focal length and diameter as shown below:

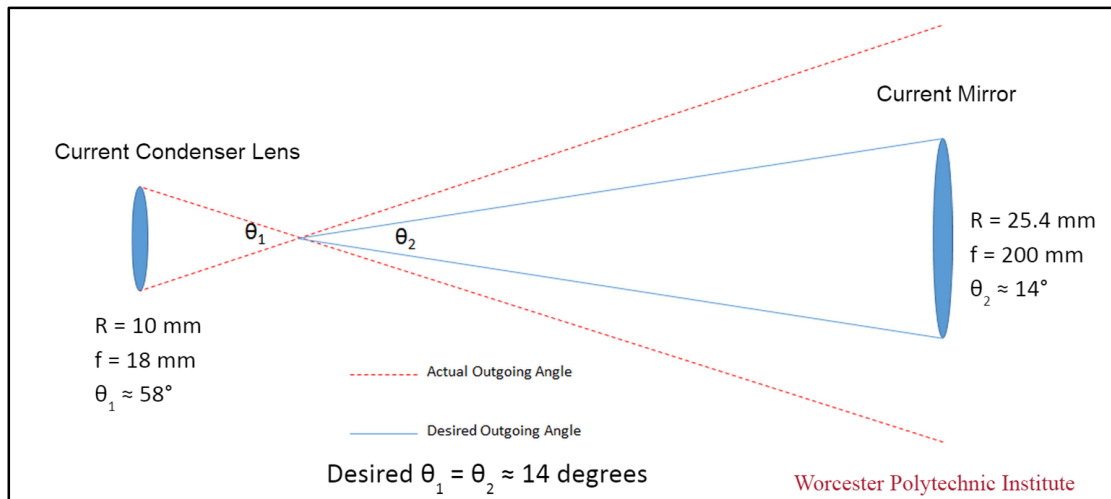


Figure 29. Old Condenser Lens Angle Comparison

In Configuration 2014.1, the slit was located at the focal point as shown in the image above. The mirror was placed 200 mm away from the slit (its focal length), which meant a large portion of light was lost due to the larger angle (θ_1 in Figure 29) produced by the condenser lens. This also meant that the mirror wasn't collimating light properly, as evidenced by the "overflow" of light from the second mirror shown on the vacuum chamber below:



Figure 30. Old System Light Collimation

Therefore, it was determined that to improve the brightness, a condenser lens that would condense the light rays at a 14° angle would be necessary to both capture all of the light and collimate the beam through the test section properly. This angle comes from the ratio between the radius R and focal length f of the mirror and is described in the equation below:

$$\theta = 2 \times \text{atan}\left(\frac{R}{f}\right) = 2 \times \text{atan}\left(\frac{25.4}{200}\right) \approx 14^\circ \quad (3.1.1)$$

If the angle is not 14°, the mirror will not collimate the light properly. Therefore, a new condenser lens was needed to provide the 14° incoming angle in order to achieve improved collimation through the test section.

Condenser Lens Selection

A new double-convex (DCX) lens was required for this application. Double-convex lenses have convex shapes on both the incoming and outgoing sides and will still focus light if the source is not perfectly collimated, but require a larger distance than published to do this. A Thorlabs LB1309 DCX lens was selected for this application. This lens has a published focal length of 7.5cm based on a collimated light source, and testing revealed the light would collimate in about 9 cm. This concept is illustrated in Figure 31 below.

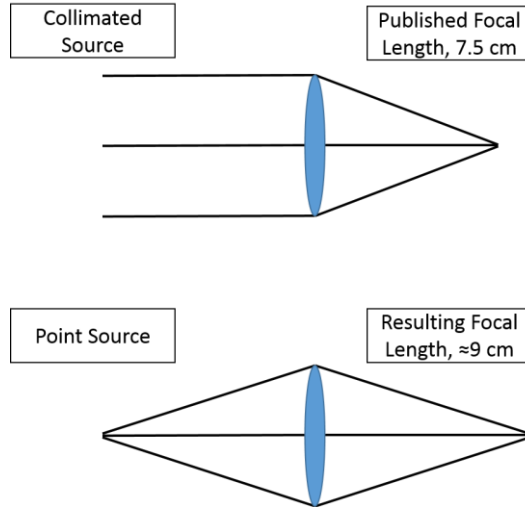


Figure 31. DCX Lens Focal Length Comparison

Calculations were made to initially test whether this lens would work, but finalized distances were based on extensive testing in the lab. These distances are summarized in Table 2 below.

| Description | Distance | Comments |
|-------------------------------------|----------|------------------------------------------------------------------------------------------------------------------------------------------------------------------------------------------------------------------------------------------------------------------------------------------------------------------------------------------------------------------------------------------------------------------------------------------------------------------------------------------------------------------------------------------------------------|
| Light Source to Aspheric Condenser | 0 mm | The light radiates from the light source at a large angle. The angle of light from the light source was calculated by holding a piece of white paper a known distance from the source, and measuring the diameter of light. Using this method, the angle of light coming from the source was calculated to be approximately 40°. By placing the aspheric lens a distance smaller than its back focal length away from the incoming light, a smaller outgoing angle is achieved. This effectively narrows the angle of the light emanating from the source. |
| Aspheric Condenser to DCX Condenser | 142 mm | This is twice the back focal length of the DCX Condenser. |
| DCX Condenser to Slit | ~75mm | This is the published focal length of the DCX Condenser lens that allows it to focus on the slit. |
| Slit to Mirror | 200mm | This is the focal length of the mirror that will allow it to collimate the light |

Table 2. Finalized First Stage Distances

Spacing Issues

Because the length of the new first stage was much longer than the previous system, there were issues with the system no longer fitting on the table. This issue was addressed by adding a flat mirror to the first stage of the system in order to reduce the straight length, which resulted in Configuration 2015.3. Because optical quality flat mirrors are expensive (roughly \$76.00 for a 2 in mirror alone [13]) an inexpensive conventional flat mirror was used to validate this concept. Using this mirror, a quality image was produced with enough space for the wind tunnel to fit in the test section.

A 1.8 in diameter Ultra Tech Round Inspection Mirror (General Tools LLC, New York City, NY) was purchased as the permanent fixture for this segment. The mirror was attached to a telescoping handle and was intended as an observation mirror for projects such as engines. This handle was affixed to a C bracket using zip ties in order to preserve the original mirror design for future use while still implementing it in the system. The mount for the flat mirror may be seen in Figure 32.



Figure 32. Flat Mirror and Mount

The collimated light from the first concave mirror was reflected into the flat mirror, which then reflected through the test section onto the second mirror, as shown in Configuration 2015.3 (Figure 28).

Slit Design

A new slit design was created to address a few issues with the previous design. First, the acrylic used in the previous slit designs was white and glossy, which ended up reflecting unwanted light onto the final projection screen. Therefore, a 10 in x 16 in x 1/8 in black P95 Matte Finish acrylic sheet was purchased from TAP Plastics (Oakland, CA) to build the new slit. Additionally, in testing it was observed that excess light would often pass the slit from the source and affect the image on the screen. Small light shields were added to either side of the slit to both improve stability and block excess light. Finally, two invertible slit orientation options were included in the assembly; one horizontal and one vertical. The horizontal slit matches a horizontal knife edge, while the vertical slit matches a vertical knife edge. The original slit design is presented in Figure 33. Updated Slit Design For reference, the bottom panel is 2 by 3 inches.

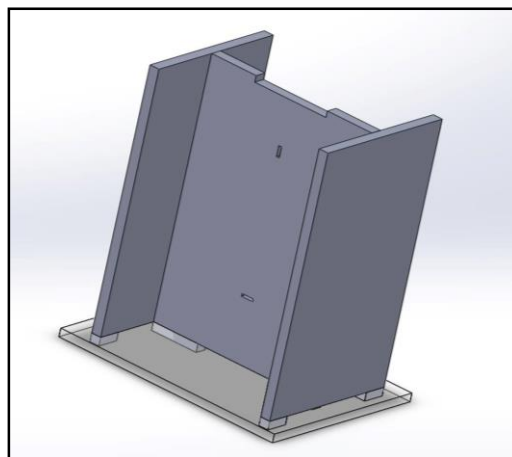


Figure 33. Updated Slit Design

The slit was laser cut from 1/8 in thick, black matte acrylic mentioned earlier. The mounts discussed later were first installed, the height of the focal point of the DCX mirror was measured, and the height of the slit was adjusted accordingly. The final, fabricated slit is shown in Figure 34.



Figure 34. Final slit design

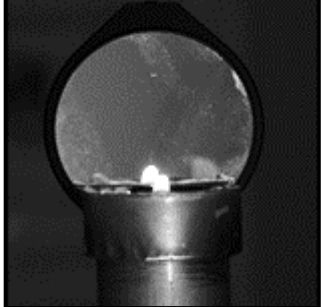
3.1.3. Image Capture

Two different methods for image capture were considered. The first continued the approach of placing the acrylic screen on the image plane and taking photos of it during testing. This was used in previous MQPs and worked as a reliable method for capture. Another method included placing the camera sensor on the image plane and focusing on the object in front of the mirror, henceforth referred to as direct image capture.

Tests to investigate direct camera image capture were conducted primarily using Configuration 2015.1, the off-axis single mirror system (See Figure 26). These tests investigated the effectiveness of capturing the image directly from the mirror. The camera used was a Canon

T3i DSLR, which was initially selected because it was available, and kept because it worked. Both capture methods were attempted with this setup. By placing the camera behind the knife edge as in Figure 44 and focusing on the object in front of the mirror, it was possible to see the schlieren images through the camera lens. However, it was difficult to actually capture these images in a photo. The best images produced are shown in Figure 35 through Figure 37. Additionally, there were some tests conducted with various camera shutter speeds in an attempt to obtain better images. It was found that using a very low shutter speed increases the amount of light that gets to the film or sensor in the camera, but with the maximum intensity of the light source, it creates an image that is too bright to be useful. Conversely, high shutter speeds let in too little light to produce an image. An investigation of shutter speeds was conducted; the extreme values are presented in Table 3.

Table 3. Initial camera capture testing results, off-axis single mirror

| Shutter Speed | Image | Comments |
|------------------|---------------------------------------------------------------------------------------------------------------------------------------------------------------------------------------|--------------------------------------------------------------------------------------------------------------------------------------------------------------------------------------------------------------------------------------------------------------------------------------------------------------------------|
| Lowest |  <p data-bbox="418 667 941 699">Figure 35. Single mirror low shutter speed</p> | Far too bright for useful information |
| Highest, 1/4000s |  <p data-bbox="418 1079 941 1146">Figure 36. Single mirror high shutter speed (1/4000 s)</p> | Too dark for useful information |
| 1/60s |  <p data-bbox="418 1491 941 1558">Figure 37. Single mirror direct capture, 1/60s shutter speed</p> | It is possible to see the schlieren image generated by the candle in the mirror; this is the best result produced. This was also edited to have +40% brightness and +20% contrast with Microsoft Word Picture Correction. Additionally, this image is not inverted, in contrast with the images projected on the screen. |

After this test, photos of the same candle flame projected into the screen using the off-axis configuration were taken. These images were taken with a shutter speed of 1/60s, and much better results were observed, as seen in Figure 37. For the sake of simplicity and because of

space constraints on the optical table, all photos outside of the direct capture test were taken from the screen. All images taken from the screen were inverted in Microsoft Word for analysis. The images taken from the screen did not reflect the quality seen in person, so further investigation into proper shutter settings was required and is discussed in the results section.

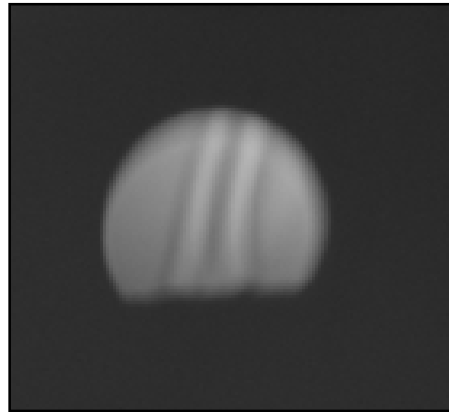


Figure 38. Screen capture test, off-axis single mirror, 1/60s shutter speed

3.1.4. System Mounting

Initial Designs and Considerations

Complex scientific optical systems often include components mounted on verniers to allow the user to make fine alignment adjustments. However, the budget available for this project didn't allow for such expensive mounting systems. To address this issue, the previous team mounted everything to a fixed aluminum optical plate, which provided stability but no options for fine-tuning the distances. A different option, 1-in X-Channel, was used heavily in testing the optimal distances between optical components for this project and previous projects, because it allowed adjustment as necessary. However, in testing, X-Channel alone was determined to be too unsteady to hold the optical components in place. A few solutions to these

issues were considered. The first was bolting the X-Channel on aluminum plate. Additionally, mounts were designed to hold the optical components more securely on top of the X-Channel. The design consisted of a $\frac{1}{4}$ -20, 1-in deep tapped hole on top a 2-in thick block of aluminum for screwing in the mirror posts. The mount was designed to be attached to the X-Channel with a $\frac{1}{4}$ -20 through-hole on the lip of the base. An example of the mounts for the first stage is seen below.

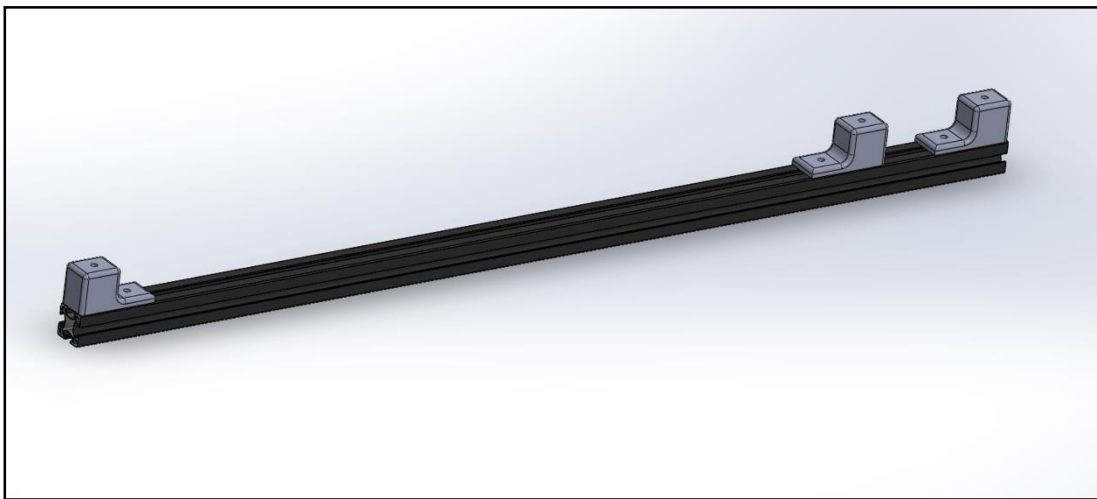


Figure 39. X-Channel Mounting System

The major disadvantage with this design was that the angular placement between mirrors would be constrained once the X-Channel was bolted down. Tilting a mirror off of its optical axis introduces aberrations such as coma that distort images, so large fine adjustments to the components were necessary. Additionally, because optical components were frequently added during testing, this system did not offer the required flexibility to function in parallel with investigative testing. Therefore, a simpler mounting system was proposed to emulate the flexibility of optical tables at low cost.

Magnetic Mounting System

A different mirror mount was designed to support the ¼-20 threaded fasteners used in previous projects. The mount was designed to use 1-¼ in diameter stock aluminum cylinder available in the Washburn shops at WPI. A ¾ in diameter, 1/8 in deep circular inset was added to the base of these mounts to house countersunk APEX (Petersburg, WV) rare earth magnets capable of producing 9.2lbs of pull force to hold the optical components to the table [14]. The mount was 1-¾ inches in height and had a ¼-20 tapped, 1 in deep blind hole in the top for the mirror posts. These were intended to be mounted on a sheet of commercially available galvanized steel. An image of the revised mirror mount design may be seen in Figure 40 below, and an image of the mirror mount in practice may be found in Figure 42.

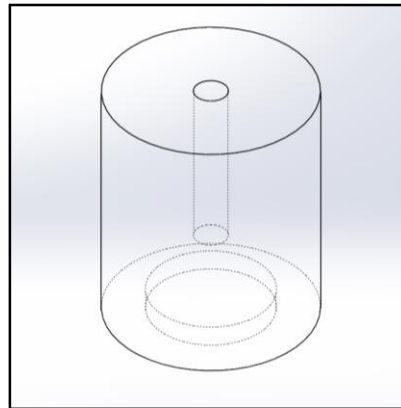


Figure 40. Magnet Mirror Mount Cutaway CAD, 1-1/4in Diameter, 1-1/2in Height

The mounts were machined in Washburn shops as discussed in Section 3.3. The insets for housing the magnets were slightly too small, so they were filed to the correct size. The magnets were affixed to the mounts using silicone caulk, as seen in Figure 41. An example of the final mount design may be seen in Figure 42.



Figure 41. Mirror mount with magnet



Figure 42. DCX Lens with new mirror mount

These mounts were originally intended to be placed on thin, galvanized steel sheets. The steel sheets were to be clamped onto the table using standard C-Clamps available from the lab. However, the material was too flexible, making alignment difficult (see Figure 43). Instead, a

second magnet was placed on the underside of the table beneath the mounts themselves. The magnets' attraction provided sufficient force to hold the mounts in place, while still enabling the user to move components around as necessary.



Figure 43. Flexible, galvanized steel sheets

3.1.5. Single Mirror Off-Axis, Configuration 2015.2

Because of the increasing complexity and size of the z-type system after adding a second lens to the first stage, a simpler alternative was considered. In early 2014, the Harvard Natural Sciences Lecture Demonstration series released an impressive video of a simple schlieren setup. This setup uses an off-axis point source of light and a single parabolic mirror placed two focal lengths away. That light is reflected back directly along the optical axis of the mirror into a knife-edge cutoff and camera similar to the third stage of the z-type system. In this system, the light passes through the test section twice. A diagram of Harvard's setup is shown in Figure 44:

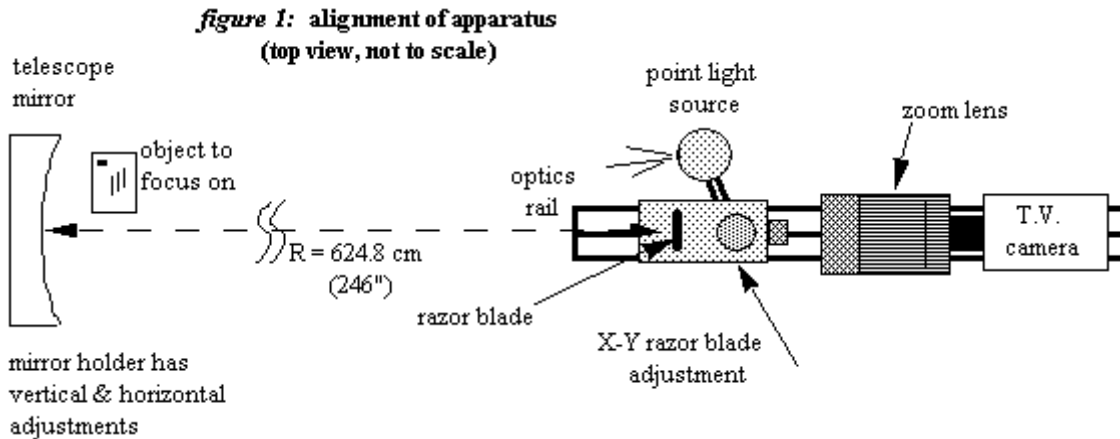


Figure 44. Harvard Natural Sciences Demonstrations single mirror setup [15] Copyright 2013 by Harvard Natural Sciences Demonstrations

This system was emulated with the existing mirror, condenser lens and slit at the point source, and a candle flame directly in front of the mirror to produce the schlieren image. A configuration for this layout may be found in Appendix 6.2. Figure 45 shows the setup that was utilized:



Figure 45. Off-axis single mirror with existing optics

In initial testing, this system produced promising results. However, it was abandoned for several reasons. First, the test section needs to be close to the mirror to produce ideal results,

which works for candles and compressed air but doesn't work well with the wind tunnel, particularly considering that the pitot probe is designed to enter through the side. Additionally, this system loses the advantage of collimated light through the test section and therefore can't be used quantitatively to measure shock and expansion wave angles. A final disadvantage to this type of system, listed in Settles' book [5], is that it produces an extremely small field of view if the mirror is small, which was also observed in testing with the 2 in mirror available.

A larger, 3 in mirror and mount was investigated for this option. Because the mounting system was designed to be flexible, if a future group wants to pursue this idea the infrastructure is available. The approximate distances and specifications for this mirror are provided in Appendix 6.2

3.2. Pitot System

The pitot system designed for this wind tunnel is a modified version of the one originally designed and implemented by the 2013 MQP. Some of the equipment and resources used by that team were to be reused for this project. The wind tunnel rebuilt by the 2014 team did not include a pitot system. Therefore, a new system that would attempt to resolve the issues previously reported by the 2013 team was to be installed. However, this installation was not performed during the course of the project.

3.2.1. Pressure Probe Installation

The stagnation pressure probe was to be a stainless steel 1/16 in OD tube bent at a 90° angle. The tip points towards the air flow and is centered within the cross-sectional area of the test section (see Figure 23). Just as the 2013 team intended, this probe was to be installed through one of the side windows of the wind tunnel so that it can be easily removed or replaced

by swapping out the window [4]. This probe was to be sealed to the window, detached from the wind tunnel, with a silicon epoxy. An alignment jig is required to accurately align the probe during installation. Therefore, a small metal fixture was designed to hold the tube in place 1-3/4 in. from the long edge of the window and 3/4 inches above its surface.

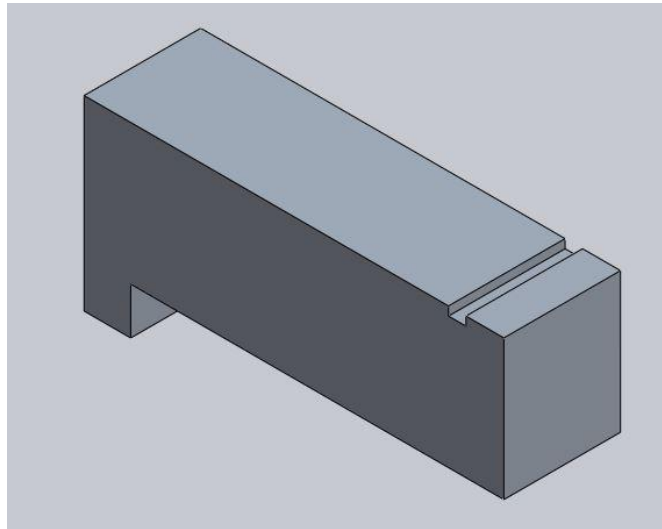


Figure 46. Probe Alignment Fixture Model, 5/8 x 1 x 2-1/4 inches

The static pressure port was to be installed in the same manner as done by the 2013 MQP team discussed in Section 2.3.5. The position of the port relative to the stagnation probe was to be determined after locating the position of the shock wave inside the wind tunnel during final schlieren system testing. This was to minimize the risk of installing the port downstream of the shock instead of upstream.

Both probes were to be connected to pressure transducers through rubber tubing. This tubing needed to be stiffer than the tubing used by the 2013 team so that it would not collapse on itself when air is evacuated by the vacuum chamber as before [4]. Due to time constraints and lack of materials, the alignment fixture could not be manufactured in time and after discussions between the team and faculty advisor, the decision was made to not pursue the

installation of either the stagnation probe or the static ports as part of the current project. The CAD model for the alignment fixture will be archived along with other project component designs.

3.2.2. Pressure Transducers

Based on the available DAQ equipment, the pitot system requires pressure transducers with an analog voltage output which indicate measured, absolute pressure. After researching and comparing several brands and models of transducers, it was decided that the ones used by the 2013 team, the Honeywell TruStability® (#HSCDANN001BAAA3) were the best choice. This model featured the lowest Total Error Band – the maximum deviation from true measurement – of all researched models and the ideal absolute pressure range (0-100 kPa) [12]. Recalling that the wind tunnel in use is an indraft tunnel with a vacuum chamber downstream, air pressure inside the tunnel should never be greater than the ambient pressure, assumed to be approximately 101.3 kPa, while the tunnel is running. The 2013 team's transducer electronics box, containing the circuitry and transducers was recovered and reused for this project. The project box includes a 12VDC Jameco DCU120050 AC/DC wall outlet transformer and a TracoPower TMR 1210 DC/DC converter to deliver ~3.3V input to the transducers [4]. The transducer electronics box is shown in Figure 47 with the cover removed.

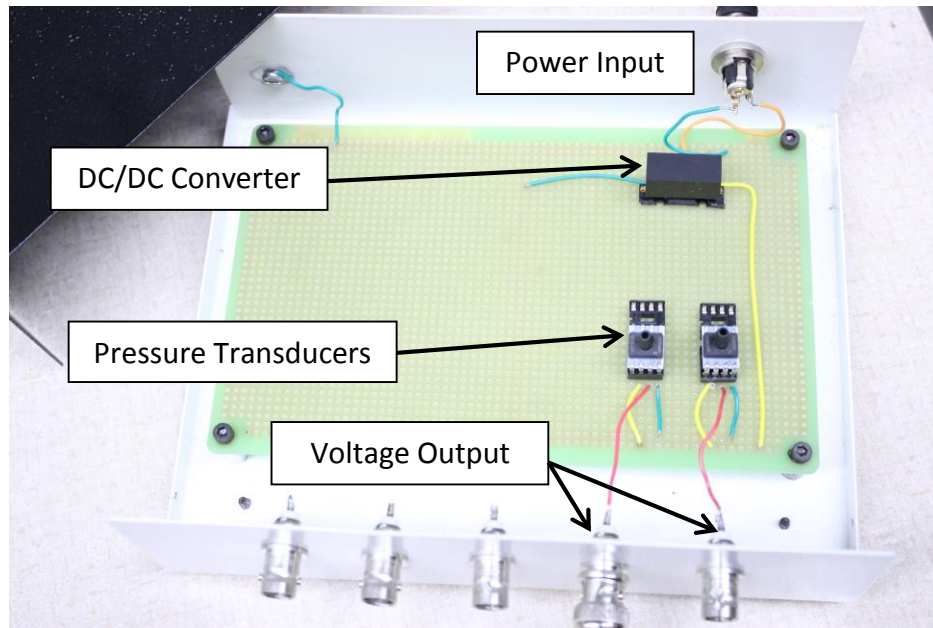


Figure 47. Pressure Transducer Circuit Box

Test Calculation

Recall that the Mach number of the tunnel air flow is to be calculated from the pressure measurements. Test calculations were run to determine the worst-case Mach number error resulting from uncertainties in the transducer measurements – the “Total Error Band.” The calculations included the use of the isentropic flow relations, Rayleigh Pitot equation, and transducer transfer functions (Equations 2.3.3, 2.3.5, and 2.3.10-11 respectively) as well as the assumption of a 3.3 V supply voltage to the system. See Appendix 6.1 for the full walkthrough of the following calculations.

For a Mach 4.0 flow, the isentropic flow and normal shock relations predict an expected static pressure of $P_1 = 0.67$ kPa and a stagnation pressure $P_{02} = 14.06$ kPa. The transducers then supply to the data acquisition system corresponding voltages of $V_{p1} = 0.3476 \pm 0.0264$ V and $V_{p02} = 0.7012 \pm 0.0264$ V. The LabView display which is part of the DAQ system will convert these back to pressure values as $P_1 = 0.67 \pm 1.00$ kPa and $P_{02} = 14.06 \pm$

1.00 kPa. According to the static pressure result, it is possible for the system to measure this pressure as zero, making it unable to properly calculate the Mach number. For a static pressure near zero, the resulting Mach number becomes greater than 10; however, for a pressure of $P_1 \gtrsim 0.42$ kPa, the corresponding Mach number will be $M \approx 4.0 \pm 1.6$. This worst-case uncertainty in the Mach number is unacceptable because at a Mach number of 4.0, an uncertainty of ± 1.6 could indicate the wrong flow regime. Then again, this result is based on the Total Error Band which represents the worst possible error, while the nominal measurement accuracy is supposedly only 0.25% Full Scale Span [12].

For $M = 2.0$, the expected pressure measurements are $P_1 = 12.95$ kPa (0.6719 V) and $P_{02} = 73.04$ kPa (2.2583 V). The voltage and pressure measurement uncertainties will be the same as in the previous case, but the resulting Mach number uncertainty will instead be ± 0.1 . The lower the pressures in the running wind tunnel, the larger the expected Mach number error. It may be difficult if not impossible for the current planned pitot system to provide reliable data from wind tunnel tests simulating Mach 4 and higher flows. This is an issue that can be addressed in a future project.

3.2.3. Data Acquisition System (DAQ)

Several revisions were made to the LabVIEW virtual instrument, or “VI” from the 2013 group, and the results from the pressure transducer circuitry were improved. These revisions are discussed in the sections below.

LabVIEW Revisions

The data collection LabVIEW code, based on the 2013 MQP group’s code, was rebuilt from scratch with the most significant changes made to both the transfer function relating voltage to

pressure and the Mach number solvers. Additionally, a function for exporting time, pressure, and Mach number data to a comma-separated values (.CSV) file was added. Each new feature is described in detail in the following section.

Data Collection

The original VI from the 2013 MQP team collected data at a sampling rate of 1 kHz, and read 100 samples. This meant that the sample buffer size was 100 samples. The sampling rate for the new VI was updated to 100 samples per second to correspond to the buffer size, otherwise the DAQ Assistant settings remained the same.

The sample rate was used to calculate the corresponding run time for each sample. This was done by specifying a sampling rate ($.01 \text{ s}^{-1}$) for each sample within a “full loop iteration” used to generate a 100x1 array. Each loop iteration corresponds to one second of test time. Figure 48 below shows the DAQ Assistant block, signal split, and the test time calculation loop.

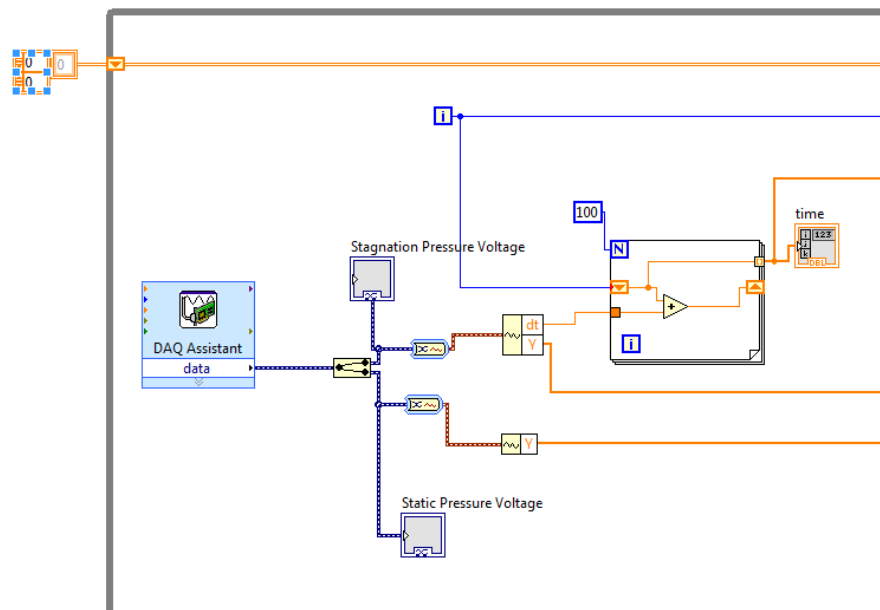


Figure 48. DAQ Assistant and Time calculation

Voltage Transfer Function

The voltage conversions were originally calculated using the built-in mathematical operators in LabVIEW. The new VI uses MATLAB scripts embedded in the code to calculate the pressures from the input voltages. When the VI is opened, a MATLAB command window is also opened and must remain open for the scripts to work. Whenever a MATLAB script is used, the inputs are passed from LabVIEW to the MATLAB script server where the calculations are performed and returned to LabVIEW. The MATLAB transfer function code is shown in Figure 49. The calculated voltages are stored as a 100x1 column array of complex numbers, which is a data type in LabVIEW. The numbers are stored as “complex” because the variables sometimes fail to be sent to the MATLAB script server when they are passed from LabVIEW into MATLAB as “real” type variables [16]. The pressures calculated from the transfer function script are then passed into an indicator on the front panel. Another MATLAB script uses the Newton-Raphson method, discussed in the following section, to solve for the Mach number.

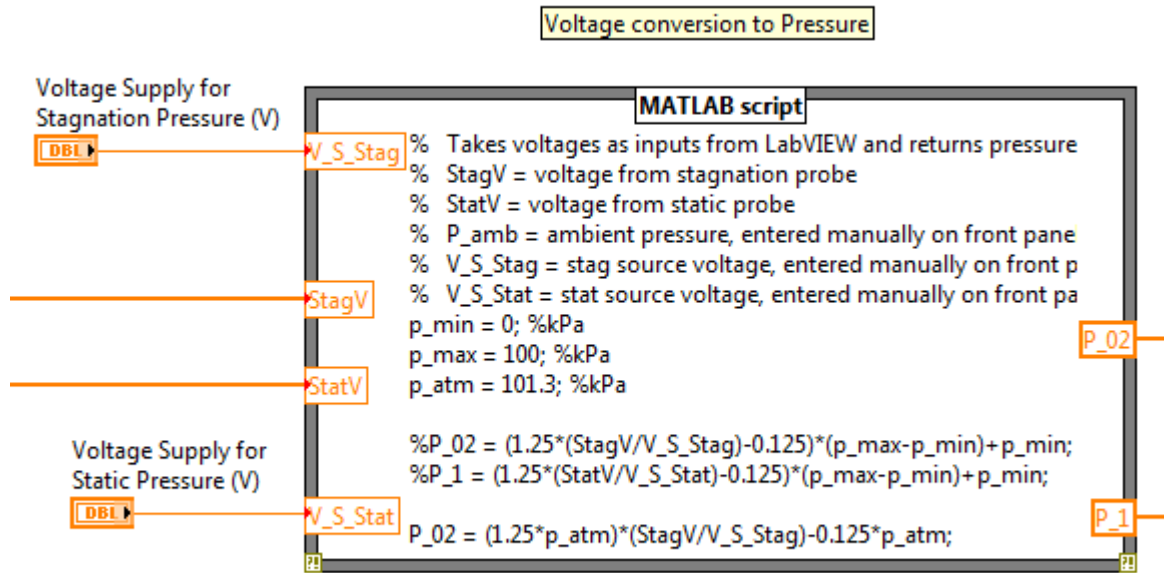


Figure 49. LabVIEW Voltage Transfer Function

Numerical Solving Method Selection

Two different methods for solving the Rayleigh Pitot Formula in MATLAB were explored. The first was using 'fsolve', a built-in MATLAB function for solving non-linear equations. However, using fsolve in MATLAB requires optimization options to be enabled, which cannot be done in a script that is called from LabVIEW. Therefore, the Newton-Raphson method was favored over the MATLAB fsolve function.

The Newton-Raphson method, as discussed in Section 2.3.2, requires a guess for the Mach number value to begin the iterative solution. This guess is a constant that is entered on the front panel of the VI, as seen in Figure 50 below.

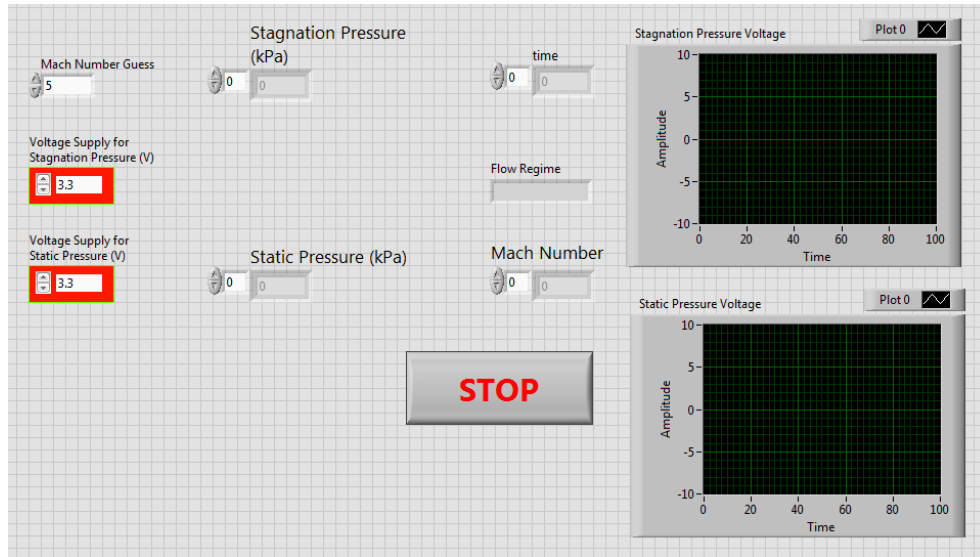


Figure 50. Final LabVIEW Front Panel

The specific heat ratio γ was taken to be 1.4. A Boolean function was used in the 2013 VI to determine the flow regime (subsonic or supersonic) and therefore how the Mach number was calculated. A subsonic Mach number was to be calculated if the difference between ambient pressure and measured stagnation pressure was between -5 and 20 Pa; otherwise, a supersonic Mach number was calculated [4]. In the new VI, the flow regime is determined by comparing the calculated pressure ratio to the critical pressure ratio (see Equation 2.3.6). The function for this is included in the MATLAB code, as shown in Appendix 6.5. The LabVIEW implementation may be seen in Figure 51. The test process for this refined code is outlined in the following section.

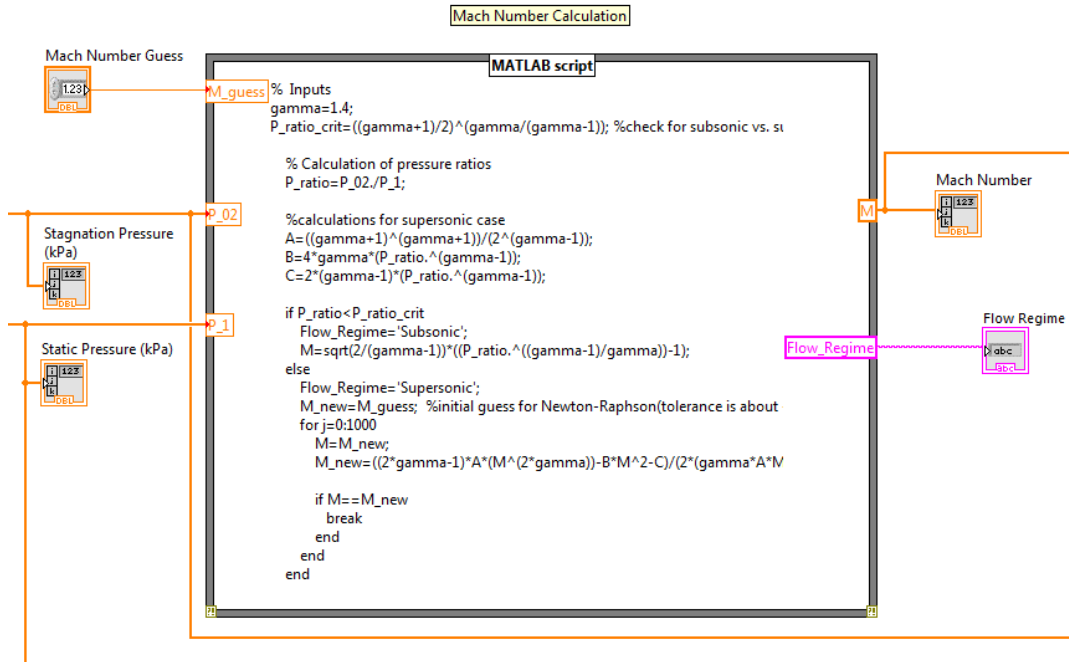


Figure 51. Newton Raphson Solver in LabVIEW

3.2.4. Test of DAQ System

The first series of tests excluded the pressure transducers and instead applied power directly to the NI USB-6009 DAQ card to simulate voltage outputs from those transducers. These tests were intended for checking the accuracy of the system's Mach number calculations.

Test Setup

The simulated voltages were produced by BK Precision 1620A and Sorensen XT 15-4 power supply units, each with the negative output channels grounded. Fluke 83III and WESTWARD 91 multimeters were connected in parallel between each power supply unit and the DAQ card. The multimeters more accurately displayed the voltage inputs to the system. The input for the stagnation pressure readings was connected to the AI0 (AI0+) channel on the DAQ card with the corresponding negative channel, AI4 (AI0-), grounded. The input for the static

pressure was similarly connected to the AI3 (AI3+) and AI7 (AI3-) channels. The setup is illustrated in Figure 52 and Figure 53 below.

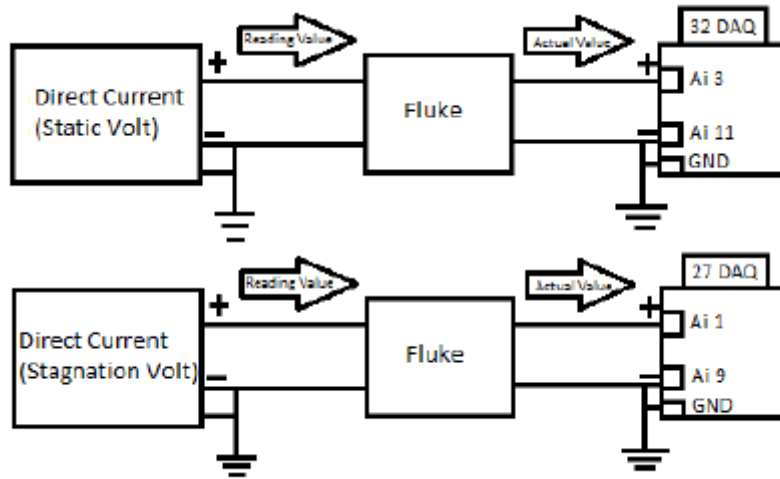


Figure 52. Test Setup Reference Diagram [4] Copyright 2013 by William Bugden et al.



Figure 53. Initial Test Setup



Figure 54. DAQ Card Channel Inputs

Initial Testing

Dozens of tests were run to debug the LabVIEW VI. Of these tests, two produced results in which the accuracy of the Mach number calculations could be evaluated. ‘Test A’ was performed when the VI was only a slightly modified version of the 2013 MQP group’s code. ‘Test B’ was performed after the MATLAB scripts were embedded into the VI. The results are displayed below.

| | Expected Mach number | Input Voltage V_1 | Input Voltage V_{02} | Output Mach number |
|--------|----------------------|---------------------|------------------------|--------------------|
| Test A | 2.0 | 0.672 | 2.259 | 1.358 |
| Test B | 2.0 | 0.672 | 2.259 | 2.066 |

Table 4. Initial DAQ Test Results

The Test B result is well within the ± 0.1 error expected for the Mach number calculation and demonstrates reliability of the MATLAB scripts over the previous VI’s algorithm. Although the VI was further modified following Test B, the VI continued to produce satisfactory results.

3.3. Manufacturing

This section introduces the newly designed components that were implemented for both the schlieren and pitot diagnostics. It is divided in three subsections: CAD Models, CAM Models, and Machining. The first one explains the design parameters of each of the new components with the help of Computer Aided Design (CAD) software. The second one explains the Computed Aided Manufacturing (CAM) software utilized as well as the specific tools and parameters for the machining program. Finally, the last subsection is a summary of the actual machining process that took place in the Computer Numerical Control (CNC) Manufacturing Lab in Washburn Shops at WPI.

3.3.1. CAD Models

In order to improve the quality of the images obtained with the schlieren system and the accuracy of the readings of the pitot system several components were designed. This process started with the CAD models of new parts: mirror mounts, wind tunnel side windows, alignment block, and a contour for a Mach number of 2. For all of the CAD models the software utilized was SolidWorks.

The mirror mounts' (shown in Figure 40 on page 57) objective was to hold the optical components at the same level. The main purpose was to shift from the optical plate model to a magnetic plate where parts could be more easily positioned. The mirror mounts consist of a bottom pocket where the magnets were glued and a top threaded hole where the mirrors are inserted. The bottom pocket has a diameter of $3/4$ inch and the top hole is a $1/4$ - 20 threaded hole.

The wind tunnel side windows were based off the previous MQP, but the positioning for the holes were incorrect so the design had to be revised. The new CAD model consists of the correct positioning of the holes for attaching the side window to the wind tunnel. New side windows were necessary because in previous years, the teams had manufactured these from acrylic. When screws in this material are tightened, the acrylic showed some evidence of cracks which interfered with the optical quality of the schlieren system. The dimensions for the clearance holes were kept the same, i.e. to accommodate the (¼-20 in) mounting bolts, and the new material selected was polycarbonate.

The alignment block (shown in Figure 46 in page 62) was designed in order to correctly position the stagnation probe in the direction of the flow to get correct measurements. This block was designed to rest against one of the side windows and also the bottom surface of the tunnel's test section. The block has a small channel (width of 3/32 in. and depth of 1/32 in.) for the probe to rest in while it is being glued to the tunnel.

The final part designed was the contour for a Mach number of 2. The decision to change from the dual-bell nozzle to the one with Mach number of 2 was due to the fact that the pressure transducers would not be able to give any accurate readings with the dual bell nozzle which produces a Mach number of 4. The CAD model was based off of previous MQPs that worked with the $M = 2$ contour with some small adjustments, for example, new holes for the static probe.

3.3.2. CAM Models

The next step in the manufacturing process was to create Computer Aided Manufacturing (CAM) models using the CAD files. The software utilized to create such models was ESPRIT. For

most of the parts there was a top and a bottom operation created which simulated the machining of the component in the corresponding faces.

ESPRIT helps in terms of writing a code for the CNC Machine to run it and understand all of the operations. Additionally, one defines the tools needed for the different cuts to shape the desired part. Some of the operations include Drill Mills (DM), End Mills (EM), and Tap. The tools utilized in the four CAM models are shown in Figure 55. In the Id column you can find the name assigned to that specific tool, the No. column represents the number of tool utilized based on the numbering in the CNC Machine Shop, and the Dia./Rad. column shows the diameter of that specific tool.

| | | Id | No. | Dia./Rad. | Length Comp. | Comment |
|------|--|------------|-----|-----------|--------------|---------|
| S... | | #7 Drill | 5 | 0.201 | 5 | |
| S... | | 0.0625" | 5 | 0.0625 | 5 | |
| S... | | 1/4-20 Tap | 4 | 0.25 | 4 | |
| S... | | 3/8 DM | 6 | 0.375 | 6 | |
| S... | | 3/8 EM | 8 | 0.375 | 8 | |

Figure 55. Tools utilized in ESPRIT

After the tools are defined there are several specifications and tolerances that need to be included. These values can be easily found in the WPI CNC Machining website [17]. in several tables depending on the type of tool used.

Finally the CAD models are imported into the ESPRIT software and the desired solid is oriented with respect to the XYZ coordinate system. On one of the faces, “chains” are created; these chains represent the area where the tool is going to interact with the stock material. A chain is utilized in ESPRIT to show the path the tool is going to take in the actual machining. For each chain there is a tool assigned to it as well as a machining command such as “Drill”, “Pocket”, etc. With this last step a simulation is shown, just to make sure that every step is correct. This

simulation consists of a 3D animation of the part that is being machined; then the tools appear in the specified order, and start making cuts.

3.3.3. Machining

The final step of the manufacturing process was the machining of the components in the CNC Manufacturing Lab at WPI's Washburn Shops. For the contour and the alignment block, the CNC Manufacturing Lab ran out of stock material and due to time constraints the team was not able to order the material therefore these parts were not machined.

Six blank cylinders of 1.5-in diameter were provided for machining the mirror mounts. Then he guided the team on how to use The vertical mold machine (VM2) was utilized to manufacture parts aligned in the z-axis. For the side windows the process was similar with the only difference that the stock material was provided by the team. After having these parts manufactured, the next step was to glue the magnets to the bottom of the mirror mounts. Unfortunately the machines tend to have a small error so the magnets didn't fit; our solution was to file the extra metal until the magnets were in place.

3.4. Qualification Test Plan

The following section provides recommended test specifications for future qualification testing to validate the diagnostics for the supersonic wind tunnel. Due to time constraints, this was not implemented during the course of this project. The purpose of this qualification process is to establish the academic value of the "Wind Tunnel and Diagnostics Project" as a future tool for teaching. This qualification test plan provides an assurance to WPI Faculty that the wind tunnel is properly functioning compared to a set of standards.

If any modification is done to the wind tunnel and/or its diagnostics, the qualification test plan has to be completed again to prove the system still meets the established standards. The following section introduces intended test specifications.

Features to be tested

The features that are going to be tested in the qualification process are listed below. These features have been ranked in level of importance from highest to lowest with respect to their academic value. Here, academic value means qualitative and quantitative results from the diagnostic systems can be used to draw conclusions from wind tunnel tests. Additionally there is a brief description on why we decided to test this feature.

- **Test Section Mach Number Reading:** Important in order to compare the Mach number obtained from the LabVIEW program with the contour's theoretical Mach number.
- **Stagnation Pressure Reading:** Important in order to establish a relationship with static pressure reading to confirm the Mach number obtained. It also confirms that the stagnation probe and its connections are working.
- **Static Pressure Reading:** Important in order to establish a relationship with the stagnation pressure reading to confirm the Mach number obtained. It also confirms that the static port and its connections are working.
- **Shockwave Schlieren Image:** Important in order to illustrate an accurate image of what is going on inside the test section.

Additionally, there are other features that are going to be tested that impact the results of each system. These features are conditions necessary to have a correct flow throughout the test section.

- **Leakage:** The existence of leaks means the test data is likely not accurate.
 - In the attachment to the vacuum chamber
 - In the wind tunnel side panels
- **Unexpected Vibrations:** The existence of vibrations can make the system unstable, like the optical components falling.

Features not to be tested

Some features are not going to be tested because they are assumed to be correct and pretested before the qualification process. The features that are not going to be tested are:

- Schlieren Components Spacing
- Schlieren Components Alignment
- Stagnation Probe Alignment
- LabVIEW Program

Hardware

This qualification test requires the following hardware components:

- Vacuum chamber facility
- Supersonic wind tunnel
- Schlieren system
- Pitot system
- Computer
- Camera

Software

The software required for this qualification test is LabVIEW and the program has already been written by the group in order to find the Mach number in the test section based on measured static and stagnation pressures.

4. Results

4.1. Schlieren System

Test Plan and Results

Several tests were completed with evolving configurations for the schlieren system. First, the system in its original configuration was tested with a candle to validate improvements in image quality. Because the wind tunnel was not used for this test, Configuration 2015.2 was used (See Figure 27). Some light pollution resulted in image glare, so from this step it was confirmed that the screen on the system needed to face away from ambient light sources in the lab. The following table contains images from this candle test:

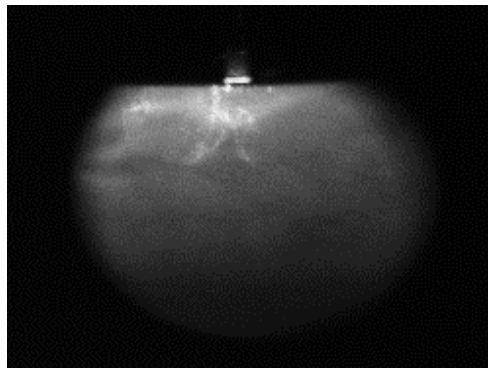


Figure 56. Configuration 2015.2 with candle, minor reflective issues

It was observed while testing in Configuration 2015.2 that adding the DCX lens to the system resulted in a large beam of focused light on the slit about 2cm in diameter, as seen in Figure 57.

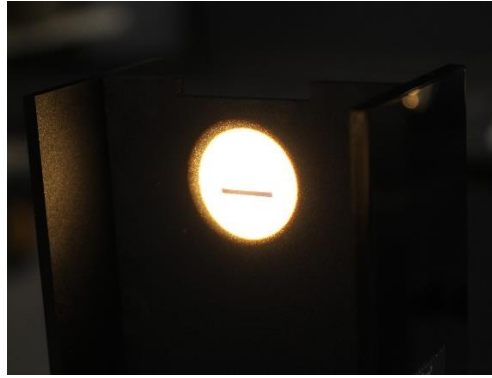


Figure 57. Light focused on slit, 2x back focal length

This meant a large amount of light was directly lost in the slit, which resulted in an observable loss of light intensity on the screen with the slit in the system as shown in Figure 58 and Figure 59.



Figure 58. Light at 2x BFL with slit



Figure 59. Light at 2x BFL without slit

Increasing the distance between the light source and DCX condenser lens resulted in a smaller focal point at the slit, which meant light was no longer cut off. This may be observed in Figure 60.

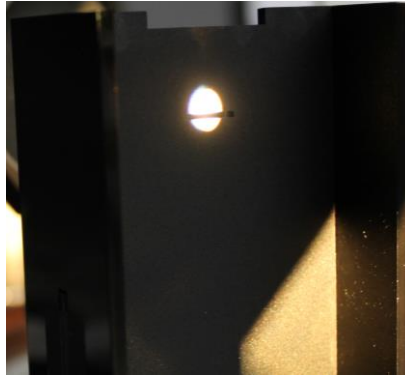


Figure 60. Light focused on slit, 4x back focal length

Next, the system was tested in Configuration 2015.3, which included the wind tunnel and flat mirror. The final setup of Configuration 2015.3 with the wind tunnel is presented in Figure 61 below:

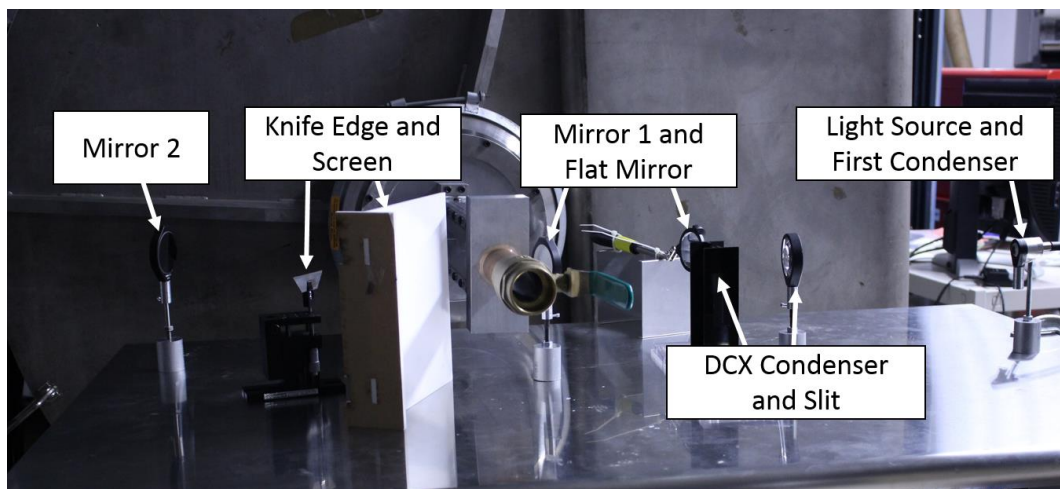


Figure 61. Schlieren Configuration 2015.3 Setup

This configuration was again tested with a candle to first verify that it still produced similar image quality even with a component added to the system. The results of adding the flat mirror to the system can be seen in Figure 62:

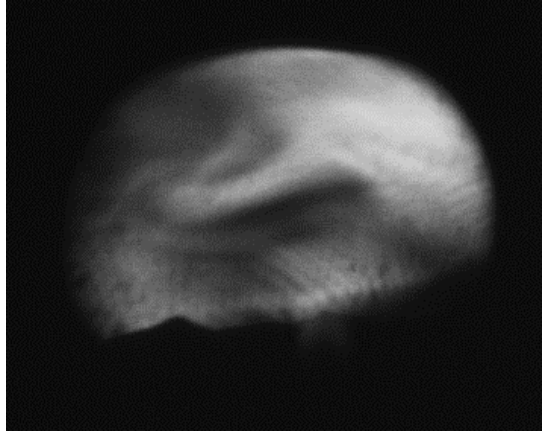


Figure 62. Image with flat mirror with +40% contrast

Figure 62 shows interference of air blown through a straw with heat rising from a candle. The image displayed in the report was inverted from the original image taken from the screen. This image is much clearer than Figure 38, which was the best image taken from Configuration 2015.1.

Finally, the schlieren system was tested with the dual bell nozzle contour in the wind tunnel in Configuration 2015.3. These were compared to theoretical schlieren images created by the 2014 MQP team using post-processing in Fluent, seen in Figure 57 below.



Figure 63. Fluent Schlieren Image at a pressure ratio of 10 [1] Copyright 2014 by Katlin Davis et al.

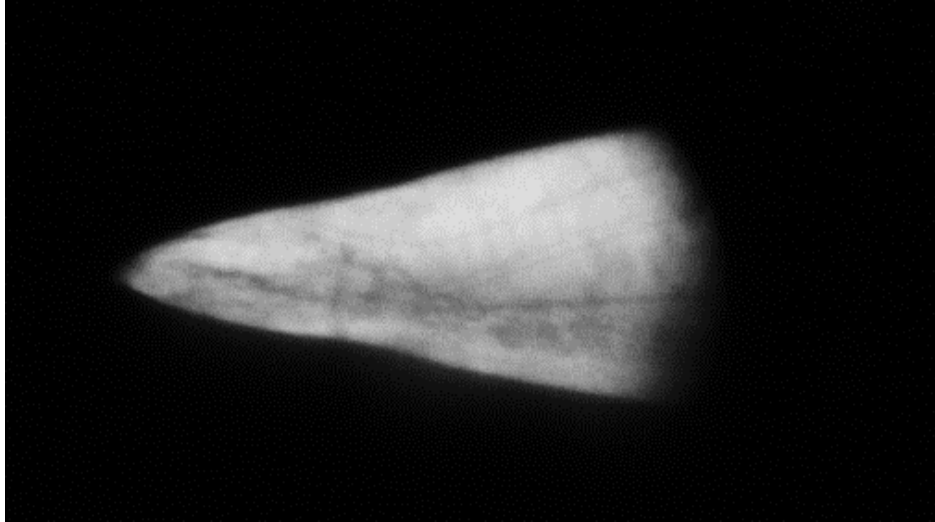


Figure 64. DBN Schlieren Test, Lower Contrast

For the first test, photos were taken at a pressure ratio (chamber to ambient) of about 10 as approximated by the vacuum chamber readings, and a shutter speed of 1/640 s. The image in Figure 64 has been inverted and edited in Microsoft Word to add +20% brightness and +40% contrast. It is difficult to see the flow structures predicted by the computational model in this image, largely because of the low contrast. To improve the contrast of the image, the test was run again at a similar pressure ratio with the knife edge raised higher to cut off more light, providing higher contrast. The result may be seen in Figure 65 , again modified in Microsoft Word with +20% brightness and +40% contrast.

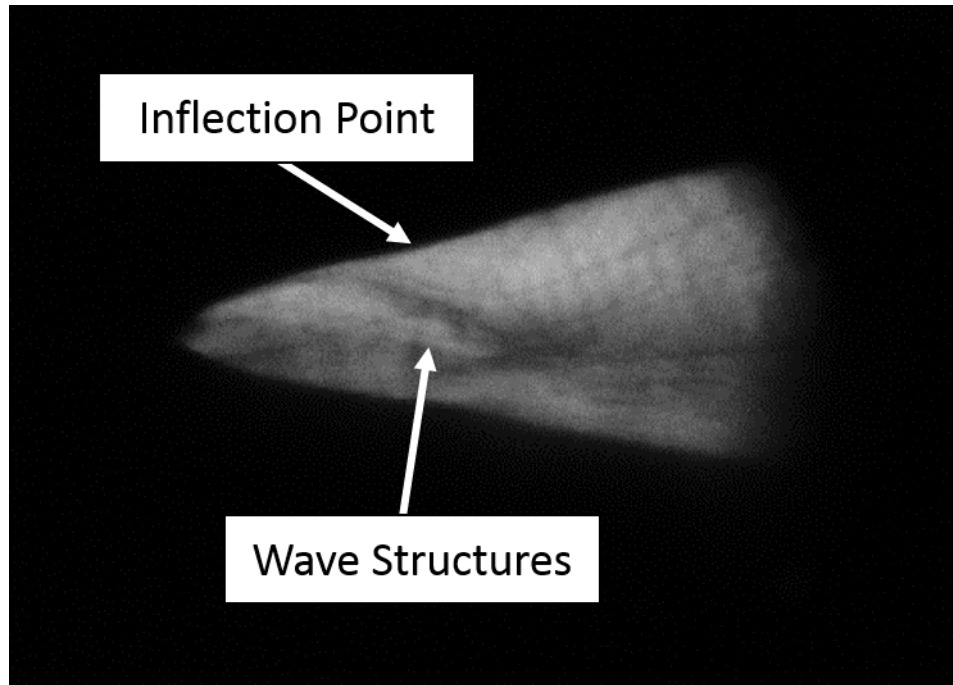


Figure 65. DBN Schlieren Test, Higher Contrast

There is a large improvement in contrast with this image over Figure 64, which was achieved by raising the knife edge slightly. It is possible to see waves which propagate away from the walls upstream of the inflection point of the dual-bell nozzle, as predicted by the CFD model in Figure 63.

4.2. Pitot System

Due to time constraints, the system was not tested with the wind tunnel. The latest set of tests involved using the pressure transducer electronics box designed by the 2013 MQP team. The circuit was connected to a wall power outlet, and the transducers were connected to the appropriate channels on the DAQ card using long, single-core copper wires. The circuit box setup may be seen in Figure 47.

Initial testing revealed that the static pressure transducer was not receiving power from the power source. This was diagnosed using a multimeter with the circuit box powered. The

yellow wires correspond to the input power for each transducer. The stagnation transducer input was reading a steady 3.3V, but the static transducer was not receiving power. The transducer box was taken apart and the power leads for the static transducer were re-soldered, solving this issue. After the repairs, the input voltage for both transducers was a steady 3.3V as expected, so the power source was confirmed to be reliable.

The pressures calculated from the voltages read by the DAQ card were much lower than expected for ambient pressure. According to the transfer function, the expected output voltage for ambient pressure should be just under three volts. A Python script was written to calculate expected pressure readings versus the theoretical signal voltage output range for the transducers, and the output of the function is shown in Figure 66.

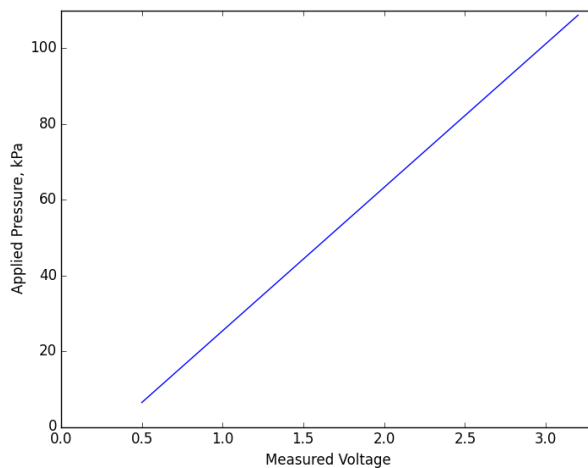


Figure 66. Expected pressure-voltage relation

The voltage recorded in LabVIEW when the pressure transducers are at ambient pressure was about 1.4-1.5V, which resulted in pressure readings around 41 kPa. A multimeter was again used to measure the signal output from the transducers to make sure the issue was not related to the DAQ card. The signal output for both transducers was similarly 1.4-1.5V, suggesting there may be a problem with the transducers. A correction factor could be applied to the pressure

transfer function to compensate for this issue, or new, replacement pressure transducers could be purchased.

4.3.Recommendations for Future Work

Significant progress was made in assessing and designing diagnostic systems for the supersonic wind tunnel, but there are several improvements that can be made by future groups.

4.3.1. Schlieren System

Mounting System Design

The optical mounting system designed for this project had both advantages and disadvantages. One advantage was flexibility in adding and moving components. With the previous mounting systems, there was no option for moving components in the x-y plane either because they were attached to X-Channel or an aluminum plate. The flexibility enabled adjustments while testing.

There were also several disadvantages to this mounting system that should be addressed in future projects. For example, the height of the machined aluminum mirrors mounts made the mirrors too tall with the existing posts and ball and socket mounts. The ball and socket mounts provided adjustments in pitch in case there were imperfections in the mounting plate or aluminum mounts, so needing to remove them also removed flexibility in pitch. The mirrors can still be adjusted in height by unscrewing them from the threaded aluminum mirror mounts and fastening them in place with a nut, however, it would be ideal to be able to incorporate the ball and socket mounts for the mirrors again. Component height could be reduced by cutting the threaded posts, reducing the adaptor collar height, or reducing the aluminum mount height.

Additionally, the backwards pull force of the light source cord is too great for the glue to hold the magnet inside the mount. Occasionally, the mount would tip over and the magnet would remain affixed to the table, meaning the magnets were sufficient but the glue was not. Therefore, a system for holding the light source gooseneck wire should be designed so the tension is placed on the holder and not the light source mount.

There are a few ways the slit can be improved. Despite the measurements, the slit is about a half inch too short in height. This can be corrected by raising the base of the slit on other materials, but it would be ideal to have the slit support itself. Additionally, mounting tabs could be added to the top of the side panels in order to make it so they don't need to be removed when the slit is flipped for a different configuration.

Finally, a better method for attaching the aspheric condenser lens to the light source mounting collar should be designed. Some optical systems use breadboards for mounting components as well, so $\frac{1}{4}$ -20 holes could be machined into the existing aluminum sheet from the 2013-2014 project to maintain the height the ball and socket mounts were designed for, while still providing options for component movement. This could also address some of the stability issues introduced by the light source cord.

4.3.2. Pitot System

With the LabVIEW VI working, the next step is to test the pressure transducer output to ensure that they read the proper values. Such a test will most likely involve the use of a calibrated barometer that can be trusted to serve as a reasonable standard. Correction factors may need to be added to the LabVIEW calculations to account for any offsets in voltage readings. The alignment fixture and Mach 2 contour (or any additional contour of choice) must be machined

using the CAM files created in this project. The pressure probes still need to be installed into the wind tunnel, and final testing of the system with the running wind tunnel must be performed. The wind tunnel may also have to be reexamined for possible leaks that may have developed since the last use.

5. References

1. Davis K, Fortner E, Heard M, McCallum H, Putzke H. Experimental and Computational Investigation of a Dual-Bell Nozzle. Worcester; 2014. Report No.: JB3-DNB1.
2. Butler K, Cancel D, Earley B, Morin S, Morrison E, Sangenario M. Design and Construction of a Supersonic Wind Tunnel. Worcester: Worcester Polytechnic Institute - JB3-SWT2; 2010. Report No.: JB3-SWT2.
3. Moore P. Design of a Supersonic Wind Tunnel. Worcester: Worcester Polytechnic Institute; 2009. Report No.: ME-JB3-SWT1.
4. Bugden W, Fitton K, Folinas G, Fournier N, Hogan G, Ito M, et al. Design and Construction of a Supersonic Wind Tunnel with Diagnostics. Worcester: Worcester Polytechnic Institute ; 2013. Report No.: JB3-SWT3.
5. Settles G. Schlieren and Shadowgraph Techniques: Visualizing Phenomena in Transparent Media New York: Springer-Verlag; 2001.
6. Krake V, Bauer B. Schlieren Photography. [Online].; 2003 [cited 2014 October 14]. Available from: <http://mxp.physics.umn.edu/s03/projects/s03schlieren/newpage3.htm>.
7. National Air and Space Administration. NASA Glenn Research Center. [Online]. [cited 2014 October 14]. Available from: <http://www.grc.nasa.gov/WWW/k-12/airplane/pitot.html>.
8. MIT Unified Engineering. Shock Losses, Compressible Flow Pitot-Tube Lecture Notes. [Online].; 2007 [cited 2014 October 14]. Available from: <http://web.mit.edu/16.unified/www/SPRING/fluids/Spring2008/LectureNotes/f16.pdf>.
9. Anderson JD. Fundamentals of Aerodynamics. 5th ed. New York, NY: McGraw-Hill; 2011.
10. Devenport WJ. Compressible Aerodynamics Calculator. [Online].; 2014 [cited 2015 March 18]. Available from: <http://www.dept.aoe.vt.edu/~devenpor/aoe3114/calc.html>.
11. Farris MH, Russel CT. Determining the Standoff Distance of the Bow Shock: Mach Number Dependence and Use of Models. Journal of Geophysical Research. 1994; 99: p. 17,681-17,689.
12. Honeywell. TruStability Silicon Pressure Sensors: HSC Series-High Accuracy [Product Specification].].
13. Thorlabs. [Online].; 2014 [cited 2014 December 10]. Available from: http://www.thorlabs.com/newgrouppage9.cfm?objectgroup_id=141.

14. 3/4" x 1/8" Disc - North Pole Marked - Neodymium Rare Earth Magnet. [Online].; 2014 [cited 2014 December 16]. Available from: <http://www.apexmagnets.com/3-4-x-1-8-disc-north-pole-marked>.
15. Harvard Natural Sciences Demonstrations. Harvard Faculty of Arts and Sciences. [Online]. [cited 2014 December 9]. Available from: <http://www.fas.harvard.edu/~scdiroff/lds/LightOptics/SchleirenOptics/SchleirenOptics.html>.
16. National Instruments. [Online].; 2014 [cited 2015 February 5]. Available from: <http://digital.ni.com/public.nsf/allkb/2B3FF46C8512C4F786256CF30071BE53>.
17. Worcester Polytechnic Institute Manufacturing Laboratories. Feeds and Speeds. [Online]. [cited 2015 March 18]. Available from: <https://sharepoint.wpi.edu/research/CNCLabs/SitePages/Feeds%20and%20Speeds.aspx>.
18. Ch. 11 - Optics Part 2. [Online].; 2004 [cited 2014 November 18]. Available from: <http://www.physics.uc.edu/~sitko/LightColor/11-Optics2/optics2.htm>.
19. United States Air Force. Performance Flight Testing Vol. I Edwards Air Force Base: Air Force Material Command; 1991.
20. The Engineering Toolbox. [Online]. [cited 2015 February 4]. Available from: http://www.engineeringtoolbox.com/standard-atmosphere-d_604.html.

6. Appendices

6.1. Test Calculations of Mach number Error for Honeywell #HSCDANN001BAAA3 Pressure Transducer

1. Determine P_1 and P_{02} for expected $M_1 = 4.0$ and $\gamma = 1.4$

a. Use isentropic flow relations to find P_1 from $P_{01} = 101.325$ kPa

$$\text{i. } \frac{P_{01}}{P_1} = \left(1 + \frac{\gamma-1}{2} M_1^2\right)^{\frac{\gamma}{\gamma-1}}$$

$$\text{ii. } P_1 = 0.67 \text{ kPa}$$

b. Use normal shock relations to find P_{02}

$$\text{i. } \frac{P_{02}}{P_1} = \left(\frac{\gamma+1}{2} M_1^2\right)^{\frac{\gamma}{\gamma-1}} / \left(\frac{\gamma+1}{1-\gamma+2\gamma M_1^2}\right)^{\frac{1}{\gamma-1}}$$

$$\text{ii. } P_{02} = 14.06 \text{ kPa}$$

2. Transducer measurements

a. Use the transfer function to convert P_1 and P_{02} into voltages

$$\text{i. } V_{output} = \frac{0.8V_{supply}}{P_{max}-P_{min}} (P_{applied} - P_{min}) + 0.1V_{supply}$$

$$\text{ii. } V_{supply} = 3.3 \text{ V}; P_{max} = 100 \text{ kPa}; P_{min} = 0 \text{ kPa}$$

$$\text{iii. } V_{p1} = 0.3476 \text{ V}; V_{p02} = 0.7012 \text{ V}$$

b. From $TEB = \pm 1\%$ FSS, find the voltage measurement uncertainty

$$\text{i. } \sigma_v = 0.01 * (0.9 - 0.1)V_{supply}$$

$$\text{ii. } \pm\sigma_v = \pm 0.0264 \text{ V}$$

$$\text{iii. } \text{So } V_{p1} = 0.3476 \pm 0.0264 \text{ V and } V_{p02} = 0.7012 \pm 0.0264 \text{ V}$$

3. Converting voltages into pressure and Mach number measurements (LabVIEW)

a. Run voltages back through the transfer function to obtain the pressures and pressure measurement uncertainties

$$\text{i. } P_{applied} = \left(1.25 \frac{V_{output}}{V_{supply}} - 0.125\right) * (P_{max} - P_{min}) + P_{min}$$

$$\text{ii. } \pm\sigma_p = \pm 1.00 \text{ kPa}$$

$$\text{iii. } P_1 = 0.67 \pm 1.00 \text{ kPa and } P_{02} = 14.06 \pm 1.00 \text{ kPa}$$

1. This would have been the result had I applied the TEB to the pressure range rather than the voltage range; Step 2 was unnecessary for finding the pressure uncertainty
 2. The same method was used to translate the transducer resolution of 0.03% FSS to 0.03 kPa
- b. Run these pressures with their uncertainties through the Rayleigh equation or a compressible flow calculator to determine the worst case deviation from the expected Mach number
- i. the case involving $P_1 = 0.67 - 1.00$ kPa was very troubling; the lower limit of the transducer's pressure range is 0 kPa meaning that in the worst case, P_1 would be measured as zero or a near zero value
 1. either LabVIEW would be unable to produce a Mach number result or it would give us an impossibly high Mach number, say 16
 2. the P_1 measurement will have a large impact on our results and may be the source of significantly large errors
 - ii. for $P_1 \gtrsim 0.42$ kPa, we should have a result around $M = 4.0 \pm 1.6$
 1. the 0.42 comes from an error of 0.25% instead of 1%

6.2. Single Mirror Off-Axis Design

Single Mirror Off-Axis

This section describes parts and general dimensions researched for a single mirror off-axis system in case a future group wishes to implement the design. The following concave spherical mirror was selected for this application [1]:

Model: AX27625

Supplier: Anchor Optics

Diameter: 75mm (3 inches)

Focal Length: 150 mm

Anchor Optics also provides three-screw adjustable ring mounts that mount to any 0.5 in diameter post. The 77mm inner diameter mount is the ideal mount for this size mirror. The part number for this mount is AX36605. [2]

A rough sketch of the system may be found below:

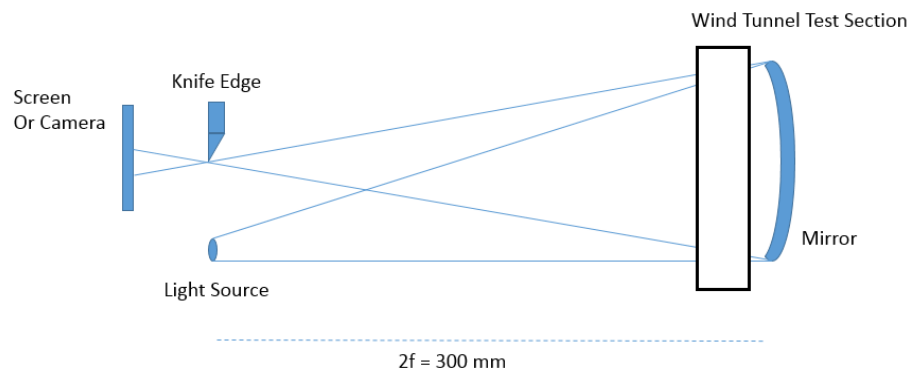


Figure 67. Single Mirror Design

Experimentation to find the proper angle between incoming and outgoing rays is required. The knife edge focus point should be in line with the light source. The method of decreasing the outgoing angle from the light source using the aspheric condenser lens could be used in this design, but would require testing. Additionally, experimentation and researched examples of these systems indicate that the wind tunnel should be as close to the mirror as feasible.

Mirror Source

Commercial Grade Large Concave Spherical Mirrors. Anchor Optics. Accessed 12/17/2014. Available from: [<http://www.anchoroptics.com/catalog/product.cfm?id=442>].

Mount Source

Three-Screw Adjustable Ring Mounts. Anchor Optics. Accessed 12/17/2014. Available from: [<http://www.anchoroptics.com/catalog/product.cfm?id=213>].

6.3. LabVIEW VI Instructions

Using the LabVIEW Program

- Open the LabVIEW VI provided by the team.
- Make sure the DAQ card is plugged into the lab computer via USB.
- Make sure the stagnation pressure probe is connected to channel 10.
- Make sure the static pressure probe is connected to channel 13.
- Press ctrl-R to start collecting data.
- Start running the when tunnel.
- When finished collecting data, press 'stop' and enter the desired file name. Be sure to include '.csv' in the file name. If you forget to do this, you can always add a .csv extension to the file name later.

The output file will look like the sample in Figure 68 below. The columns are, from left to right:

- Run time in seconds
- Mach number
- Stagnation Pressure in kPa
- Static Pressure in kPa

| | A | B | C | D | E | F | G |
|----|------|--------|--------|--------|---|---|---|
| 1 | 0 | 0 | 40.402 | 40.397 | | | |
| 2 | 0.01 | 0 | 40.45 | 40.469 | | | |
| 3 | 0.02 | 0 | 40.402 | 40.397 | | | |
| 4 | 0.03 | 0 | 40.402 | 40.397 | | | |
| 5 | 0.04 | 0.001 | 40.547 | 40.469 | | | |
| 6 | 0.05 | -0.001 | 40.402 | 40.445 | | | |
| 7 | 0.06 | 0 | 40.378 | 40.397 | | | |
| 8 | 0.07 | 0 | 40.498 | 40.469 | | | |
| 9 | 0.08 | 0 | 40.378 | 40.373 | | | |
| 10 | 0.09 | 0 | 40.474 | 40.493 | | | |
| 11 | 0.1 | 0 | 40.378 | 40.373 | | | |
| 12 | 0.11 | -0.001 | 40.378 | 40.445 | | | |
| 13 | 0.12 | 0.001 | 40.45 | 40.397 | | | |
| 14 | 0.13 | 0 | 40.45 | 40.445 | | | |
| 15 | 0.14 | 0 | 40.474 | 40.469 | | | |
| 16 | 0.15 | -0.001 | 40.305 | 40.397 | | | |
| 17 | 0.16 | -0.001 | 40.426 | 40.469 | | | |
| 18 | 0.17 | 0.001 | 40.474 | 40.421 | | | |
| 19 | 0.18 | -0.001 | 40.402 | 40.469 | | | |
| 20 | 0.19 | 0 | 40.378 | 40.349 | | | |
| 21 | 0.2 | -0.001 | 40.426 | 40.493 | | | |
| 22 | 0.21 | 0 | 40.402 | 40.421 | | | |
| 23 | 0.22 | 0 | 40.45 | 40.421 | | | |
| 24 | 0.23 | 0 | 40.426 | 40.397 | | | |
| 25 | 0.24 | 0 | 40.45 | 40.469 | | | |
| 26 | 0.25 | 0.001 | 40.426 | 40.349 | | | |
| 27 | 0.26 | -0.002 | 40.402 | 40.518 | | | |
| 28 | 0.27 | 0.001 | 40.498 | 40.421 | | | |

Figure 68. Sample LabVIEW output in Excel

6.4. Voltage Transfer Function Python Code

```
from matplotlib import pyplot

def V_to_P():
    V_S = 3.3 #Volts, supply voltage
    Voltages = []
    Pressures = []
    V_output = 0.5
    while V_output < 3.3:
        P_applied = ((1.25*(V_output/V_S)) - 0.125)*(1-0) #bar from transfer function
        Voltages.append(V_output)
        P_applied *= 100 #conversion to kPa
        Pressures.append(P_applied)
        V_output += 0.1
    ambVolt = Voltages[Pressures.index(101.1363636363637)]
    print("Expected ambient voltage: ", ambVolt)
    return Voltages, Pressures

def plotValues(x, y):
    pyplot.plot(x, y)
    pyplot.xlabel("Measured Voltage")
    pyplot.ylabel("Applied Pressure, kPa")
    pyplot.axis([0, 3.3, 0, 110])
    pyplot.title("Transfer Function Voltage vs. Applied Pressure")
    pyplot.show()

def main():
    Voltages, Pressures = V_to_P()
    plotValues(Voltages, Pressures)

if __name__ == '__main__':
    main()
```

6.5. Newton Raphson MATLAB Code

```
% Inputs
gamma=1.4;
P_ratio_crit=((gamma+1)/2)^(gamma/(gamma-1)); %check for subsonic vs.
supersonic
P_1=.1278; %atm
Plot_M = zeros(1,100); %fill Plot_M first so it doesn't waste memory resizing
Plot_PR = zeros(1,100);
for i = 1:100 %atm
    P_02 = .5*(.721)+i*.01*(.721); %atm

    % Calculation of pressure ratios
    P_ratio=P_02/P_1;

    %calculations for supersonic case
    A=((gamma+1)^(gamma+1))/(2^(gamma-1));
    B=4*gamma*(P_ratio^(gamma-1));
    C=2*(gamma-1)*(P_ratio^(gamma-1));

    if P_ratio<P_ratio_crit
        display('subsonic')
        M=sqrt(2/(gamma-1))*((P_ratio^((gamma-1)/gamma))-1);
    else
        display('supersonic')
        M_new=2; %initial guess for Newton-Raphson(tolerance is about +/-
0.5M)
        for j=0:1000
            M=M_new;
            M_new=((2*gamma-1)*A*(M^(2*gamma))-B*M^2-
C)/(2*(gamma*A*M^(2*gamma-1)-B*M));

            if M==M_new
                break
            end
        end
        end
        display(P_ratio)
        display(M)
        Plot_M(i)=M;
        Plot_PR(i)=P_ratio;
    End

figure
plot(Plot_M, Plot_PR);
xlabel('M1')
ylabel('P02/P1')
title('Mach no. vs P02/P1')
```

6.6.Fsolve MATLAB Code

6.6.1. Main Function

```
clear variables; close all; clc;
% Inputs
global g P_ratio
g=1.4;
[M0] = 1; %guess for solver
P_1=.1278; %atm

P_ratio_crit=((g+1)/2)^(g/(g-1)); %critical ratio for subsonic vs. supersonic
from 2012 MQP

Plot_M = zeros(100,1); %fill plot arrays first so it doesn't waste memory
resizing
Plot_PR = zeros(100,1);

for i = 1:100
    P_02 = .5*(.721)+i*.01*(.721); %atm

    % Calculation of pressure ratios
    P_ratio=P_02/P_1;

    if P_ratio<P_ratio_crit
        display('subsonic')
        M=sqrt(2/(g-1))*((P_ratio^((g-1)/g))-1);
    else
        options = optimoptions('fsolve','Display','iter');
        M = fsolve(@rayleighfunction,M0,options);
    end
    display(P_ratio)
    display(M)
    Plot_M(i)=M;
    Plot_PR(i)=P_ratio;
end

figure
plot(Plot_M, Plot_PR);
xlabel('M1')
ylabel('P02/P1')
title('Mach no. vs P02/P1')
```

6.6.2. Fsolve Function

```
function [ M ] = rayleighfunction( M )
%UNTITLED2 Summary of this function goes here
% Detailed explanation goes here
global P_ratio g

M = [ (((((g+1)/2)*(M^2))^(g/(g-1)))/...
      (((2*g/(g+1))*(M^2))-((g-1)/(g+1)))^(1/(g-1))))-P_ratio];
end
```